Quarterly Technical Report

Solid State Research

1987:3

Lincoln Laboratory

MASSACHUSETTS INSTITUTE OF TECHNOLOGY

LEXINGTON, MASSACHUSETTS

BEST AVAILABLE COPY

ADA192837

The views and conclusions contained in this document are those of the contractor and should not be interpreted as necessarily representing the official policies, either expressed or implied, of the United States Government.

The ESD Public Affairs Office has reviewed this report, and it is releasable to the National Technical Information Service, where it will be available to the general public, including foreign nationals.

This technical report has been reviewed and is approved for publication.

FOR THE COMMANDER

Hugh L. Southall

Hugh L. Southall, Lt. Col., USAF
Chief, ESD Lincoln Laboratory Project Office

MASSACHUSETTS INSTITUTE OF TECHNOLOGY
LINCOLN LABORATORY

SOLID STATE RESEARCH

QUARTERLY TECHNICAL REPORT

1 MAY — 31 JULY 1987

ISSUED 19 JANUARY 1988

Approved for public release; distribution unlimited.

LEXINGTON   MASSACHUSETTS

ABSTRACT

This report covers in detail the solid state research work of the Solid State Division at Lincoln Laboratory for the period 1 May through 31 July 1987. The topics covered are Solid State Device Research, Quantum Electronics, Materials Research, Microelectronics, and Analog Device Technology. Funding is provided primarily by the Air Force, with additional support provided by the Army, DARPA, Navy, SDIO, NASA, and DOE.

TABLE OF CONTENTS

LIST OF ILLUSTRATIONS

LIST OF TABLES

INTRODUCTION

1. SOLID STATE DEVICE RESEARCH

Enhancement-mode junction field-effect transistors have been fabricated in semi-insulating InP using an ion-implanted conduction channel which is modulated by a p^+-AlInAs gate grown by selective molecular-beam epitaxy. Initial devices exhibited transconductances of 26 mS/mm.

The photorefractive effect in titanium-indiffused lithium niobate waveguides has been measured by means of an integrated-optical Mach-Zehnder interferometer. The measurements were for optical wavelengths of 0.85, 1.06, and 1.3 μm, using y- and z-propagation; both photovoltaic and photoconductive effects were evaluated.

Lenslets have been formed in InP substrates by means of mass transport to smooth out chemically etched multilevel mesa structures. A 67-μm-diam. lenslet with a focal length of 80 μm has been used to collimate the output of a buried-heterostructure diode laser of 1.3-μm wavelength and has yielded a nearly diffraction-limited beam divergence of 1.4°.

A simple furnace system has been designed and successfully implemented which allows for mass transport experiments at temperatures up to 910°C without excess phosphorus accumulation and associated hazards. Large InP lenslets (120-μm diam.) have been fabricated by means of the system.

2. QUANTUM ELECTRONICS

Optically induced birefringence has been observed at 632.8 and 790.7 nm in a Ti:Al_2O_3 amplifier pumped with 10-ns-long pulses at 532 nm. The induced birefringence decays with a time constant approximating the fluorescence lifetime of the Ti^{3+} ions and is, therefore, attributed to the Ti^{3+} excited state (^2E_g) responsible for the fluorescence and gain.

Single-frequency power of 300 mW has been obtained from a Ti:Al_2O_3 ring laser pumped by 7 W (all lines) from an argon-ion laser. The laser maintains single-frequency operation while tuned from 740 to 880 nm, and its free-running frequency stability is 1.6 MHz rms with a frequency drift of $\sim$200 kHz/s.

A 10-mm-long KTP crystal has been used to frequency-double the output of a mode-locked Nd:YAG laser with greater than 50-percent efficiency, but surface damage to the crystal occurred at an unacceptably low value of 20 MW/cm^2 input intensity. The alternative of using the laser in a Q-switched mode has been found worse since mode beating led to crystal damage at lower input intensity levels than the mode-locked case.

Sodium resonance radiation has been generated with 30-percent efficiency by sum-frequency mixing the output radiation of two simultaneously Q-switched Nd:YAG lasers, one operating at 1.064 μm and the other operating at 1.319 μm. The 1.064-μm laser has also been operated as a continuous, frequency-modulated laser.

A process has been developed for growing GaAs/AlGaAs quantum wells (QWs) with controllable spatially varying thicknesses on (100)-oriented GaAs substrates. The process uses the temperature

dependence of the sticking coefficient of gallium in a molecular-beam-epitaxy system and has yielded QWs with thickness variations of over 2.5:1 at points on a wafer 1 mm apart.

3. MATERIALS RESEARCH

Superconducting thin films consisting predominantly of $YBa_2Cu_3O_x$ have been prepared by oxygen annealing of metal films formed by using electron-beam evaporation to deposit a three-layer sequence of Cu, Ba, and Y in nominally stoichiometric proportions, then repeating the sequence five times. For the best superconducting films, which were prepared on yttria-stabilized cubic zirconia substrates, the onset of superconductivity occurred at 94 K and zero resistivity was observed at 72 K.

Double-heterostructure ridge-waveguide lasers with pulsed threshold currents as low as 50 mA have been fabricated in GaAs/AlGaAs layers grown on Si by organometallic vapor-phase epitaxy. Broad-area devices from the same wafer have average threshold current densities as low as $300 \, A/cm^2$, but their laser emission occurs predominantly in a single filament.

A model that has been developed for the avalanche-induced drain-source breakdown of n-channel silicon-on-insulator MOSFETs gives calculated I-V characteristics in good agreement with experimental results. According to the model, the drain-source breakdown voltage of SOI n-MOSFETs (a) increases with increasing channel length, increasing positive substrate voltage and decreasing silicon film thickness, and (b) is higher than that of similar bulk-silicon devices at large gate bias but lower at small gate bias.

4. MICROELECTRONICS

Recent tests have shown that the previously reported 16-point discrete-cosine-transform CCD device has 60-dB dynamic range and –40-dB harmonic distortion. A new 16-point complex discrete-Fourier-transform CCD device capable of performing 10^{10} multiplications per second has been designed and is being fabricated.

The unique current-voltage relation of resonant-tunneling diodes has been used to generate high harmonics of a microwave pump frequency. Fifth-harmonic output has been obtained near 20 and 200 GHz with efficiencies of 0.5 and 0.1 percent, respectively.

Excimer laser projection has been used to pattern 130-nm lines and spaces in PMMA resist on silicon. These linewidths are significantly smaller than the 193-nm wavelength of the laser and approach the absolute diffraction-limited cutoff of the optics.

Intersubband transitions between confined states in the conduction bands of coupled quantum wells have been observed. The transition energies agree with calculated theoretical values.

5. ANALOG DEVICE TECHNOLOGY

A superconductive Josephson digital circuit has been recently designed, fabricated, and tested which provides a binary representation of the address of any of seven inputs. Circuit functionality has been demonstrated, and computer simulations predict an intrinsic processing speed of 150 ps.

Improved SAW/FET transversal filters with 100 MHz of programmable bandwidth have been fabricated. The new design, which utilizes FET conductances for tap weights, is easier to fabricate, has better uniformity, and exhibits 15 dB less insertion loss.

REPORTS ON SOLID STATE RESEARCH

1 May through 31 July 1987

PUBLISHED REPORTS

Journal Articles

JA No.

5921	Research at Lincoln Laboratory Leading Up to the Development of the Injection Laser in 1962	R.H. Rediker	IEEE J. Quantum Electron. **QE-23**, 692 (1987)
5928	Diode Lasers with Cylindrical Mirror Facets and Reduced Beam Divergence	J.N. Walpole Z.L. Liau L.J. Missaggia D. Yap	Appl. Phys. Lett. **50**, 1219 (1987)
5934	Use of Flow Visualization and Tracer Gas Studies for Designing an InP/InGaAsP OMVPE Reactor	S.C. Palmateer S.H. Groves C.A. Wang D.W. Weyburne* R.A. Brown*	J. Cryst. Growth **83**, 202 (1987)
5947	Atmospheric Remote Sensing Using a Continuously Tunable 1.7 μm Co:MgF$_2$ Laser	N. Menyuk D.K. Killinger	Appl. Opt. **26**, 3061 (1987)
5950	Stark Effect in Al$_x$Ga$_{1-x}$As/GaAs Coupled Quantum Wells	H.Q. Le J.J. Zayhowski W.D. Goodhue	Appl. Phys. Lett. **50**, 1518 (1987)
5973	Capless Rapid Thermal Annealing of Si$^+$-Implanted InP	J.D. Woodhouse M.C. Gaidis J.P. Donnelly C.A. Armiento*	Appl. Phys. Lett. **51**, 186 (1987)

Meeting Speeches

MS No.

7039A	Lithium Niobate Serrodyne Frequency Translator for Fiber Optic Gyroscopes	L.M. Johnson C.H. Cox III	In *Fiber Optics Gyros*, Proc. SPIE **719**, 141 (1987)

---

* Author not at Lincoln Laboratory.

*   *   *   *   *

UNPUBLISHED REPORTS

Journal Articles

---

* Author not at Lincoln Laboratory.

Meeting Speeches*

---

* Titles of Meeting Speeches are listed for information only. No copies are available for distribution.

* Author not at Lincoln Laboratory.

MS No.

ORGANIZATION

SOLID STATE DIVISION

A.L. McWhorter, *Head*
I. Melngailis, *Associate Head*
E. Stern, *Associate Head*
J.F. Goodwin, *Assistant*

N.L. DeMeo, Jr., *Associate Staff*

QUANTUM ELECTRONICS

A. Mooradian, *Leader*
P.L. Kelley, *Associate Leader*
A. Sanchez-Rubio, *Assistant Leader*

Aggarwal, R.L.	Le, H.Q.
Barch, W.E.	McClung, S.K.
Belanger, L.J.	Menyuk, N.
Brailove, A.A.	Schulz, P.A.
Daneu, V.	Seppala, J.P.
DeFeo, W.E.	Sullivan, D.J.
Hancock, R.C.	Tapper, R.S.
Hryniewicz, J.V.	Tong, F.F-K.*
Jeys, T.H.	Walker, W.A.
Killinger, D.K.	Wall, K.F.
Lacovara, P.	Zayhowski, J.J.

ELECTRONIC MATERIALS

A.J. Strauss, *Leader*
B-Y. Tsaur, *Assistant Leader*
H.J. Zeiger, *Senior Staff*

Anderson, C.H., Jr.	Kolesar, D.F.
Button, M.J.	Krohn, L., Jr.
Chen, C.K.	Mastromattei, E.L.
Choi, H.K.	Mattia, J.P.
Connors, M.K.	Nitishin, P.M.
Delaney, E.J.	Pantano, J.V.
Eglash, S.J.	Tracy, D.M.
Fahey, R.E.	Turner, G.W.
Finn, M.C.	Wang, C.A.
Iseler, G.W.	Young, K.K.

APPLIED PHYSICS

R.C. Williamson, *Leader*
D.L. Spears, *Assistant Leader*
T.C. Harman, *Senior Staff*
R.H. Rediker, *Senior Staff*

Aull, B.F.	Hovey, D.L.	Palmacci, S.T.
Betts, G.E.	Johnson, L.M.	Palmateer, S.C.
Bossi, D.E.*	Ketteridge, P.A.	Plonko, M.C.
Corcoran, C.J.*	Liau, Z.L.	Reeder, R.E.
Cox, C.H., III	Lieuw, S.K.*	Tsang, D.Z.
Diadiuk, V.	Lind, T.A.	Walpole, J.N.
Donnelly, J.P.	Metze, G.M.	Woodhouse, J.D.
Ferrante, G.A.	Molter, L.A.*	Yap, D.*
Groves, S.H.	O'Donnell, F.J.	Yee, A.C.

---

* Research Assistant

ANALOG DEVICE TECHNOLOGY

R.W. Ralston, *Leader*
R.S. Withers, *Associate Leader*

Anderson, A.C.
Arsenault, D.R.
Boisvert, R.R.
Brogan, W.T.
Denneno, A.P.
DiIorio, M.S.
Dolat, V.S.
Fitch, G.L.

Frickey, J.M.
Green, J.B.
Holtham, J.H.
Koulman, W.A.
Lattes, A.L.
Lichtenwalner, D.J.*
Macedo, E.M., Jr.
Munroe, S.C.

Oates, D.E.
Pan, J.Y.*
Sage, J.P.
Seidel, M.N.*
Slattery, R.L.
Thompson, K.E.
Wong, S.C.*

MICROELECTRONICS

W.T. Lindley, *Leader*
R.A. Murphy, *Associate Leader*
E.D. Savoye, *Associate Leader*
D.J. Ehrlich, *Assistant Leader*
B.B. Kosicki, *Assistant Leader*

Anderson, K.*
Astolfi, D.K.
Bales, J.W.*
Bennett, P.C.
Black, J.G.
Bozler, C.O.
Brown, E.R.
Burke, B.E.
Calawa, A.R.
Chen, C.L.
Chiang, A.M.
Clifton, B.J.
Cullen, P.A.*
Daniels, P.J.
Doherty, C.L., Jr.
Doran, S.P.
Durant, G.L.
Efremow, N.N., Jr.
Felton, B.J.

Geis, M.W.
Goodhue, W.D.
Gray, R.V.
Hollis, M.A.
Huang, J.C.M.
Johnson, B.W.
Johnson, K.F.
LaFranchise, J.R.
LeCoz, Y.L.*
Lincoln, G.A., Jr.
Lyszczarz, T.M.
Mahoney, L.J.
Maki, P.A.
Manfra, M.J.
Mathews, R.H.
McGonagle, W.H.
McIntosh, K.A.
Melngailis, J.†
Mims, V.A.‡

Mountain, R.W.
Nichols, K.B.
Pang, S.W.
Parker, C.D.
Pichler, H.H.
Rabe, S.
Rathman, D.D.
Reinold, J.H., Jr.
Rooks, M.J.
Rothschild, M.
Sedlacek, J.H.C.
Smith, F.W.*
Smythe, D.L., Jr.
Sollner, T.C.L.G.
Uttaro, R.S.
Vera, A.
Wilde, R.E.
Young, E.M.

* Research Assistant
† Part Time
‡ Staff Associate

1. SOLID STATE DEVICE RESEARCH

1.1. A p⁺-AlInAs/InP JFET FABRICATED BY MEANS OF ION IMPLANTATION AND MOLECULAR-BEAM EPITAXY

Enhancement-mode JFETs have been fabricated in semi-insulating InP substrates by means of Si^+ ion implantation to form the n-type channel region and selective molecular-beam epitaxy (MBE) of lattice-matched Be-doped AlInAs to form the p^+ gate. A cross-sectional schematic of the device is illustrated in Figure 1-1 and the detailed fabrication sequence proceeds as follows. Bare Fe-doped semi-insulating InP samples were implanted with 400-keV 5×10^{12}-cm⁻² Si^+ and annealed at 750°C for 10 min with phosphosilicate glass (PSG) used for encapsulation. Following a channel-region mesa-isolation etch and deposition of 1000 Å of plasma-enhanced SiO_2, 1.0×100-μm gates were defined and opened in the oxide by means of conventional photolithography and wet-chemical etching techniques. Prior to selective MBE growth of a 1-μm-thick layer of Be-doped AlInAs ($N_A \approx 2 \times 10^{18}$ cm⁻³) in the exposed gate region, the samples were subjected to an in-situ 20-min 400°C thermal cleaning etch with HCl gas. The growth material outside of the gate region consists of high-resistivity polycrystalline AlInAs. The InP substrates were held at a temperature of 530°C for about 1 h during the MBE growth process. Source and drain
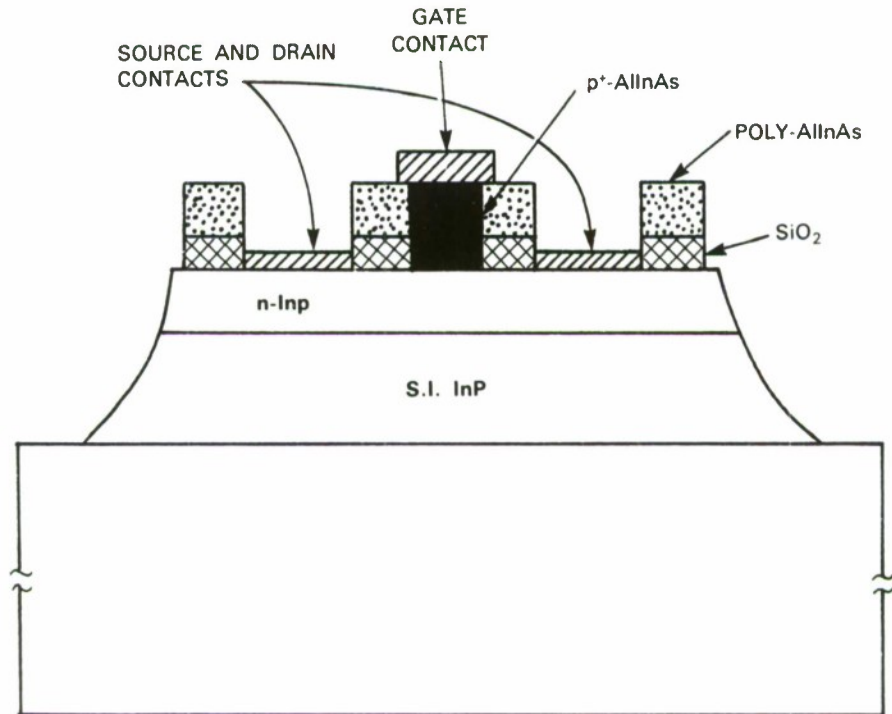
Figure 1-1. Schematic diagram of a p⁺-AlInAs/InP JFET showing the Si⁺-implanted n-InP and the MBE-grown AlInAs crystalline and polycrystalline regions.

1

contact windows were etched through the polycrystalline layers with 1:1:10 H_2SO_4:H_2O_2:H_2O and through the oxide layers with buffered HF. Electron-beam-evaporated Ni/Ge/Au and Au/Zn/Au microalloyed metals were used to contact the n and p^+ regions, respectively. Because of the presence of the high-resistivity polycrystalline layer, an oversized gate metal contact was used to ease the alignment constraints.

The zero-gate-bias channel conduction current was very low (<100 μA) on all devices, indicating that the zero-bias depletion layer very nearly extends through the 0.5-μm-thick channel region. This situation is most likely due to Be diffusion during MBE growth[1] which moves the actual p-n junction into the InP channel. Although the channel can be completely pinched off by operating these devices in the depletion mode, useful conduction current can only be obtained through reducing the depletion-layer thickness by forward biasing the gate/channel junction. Figure 1-2 shows typical enhancement-mode current-voltage characteristics of a 1.0-μm-gate-length device with a source-to-drain spacing of 5.0 μm. The gate/channel junction exhibits a reverse breakdown voltage exceeding 10 V and has a forward turn-on voltage of about 0.5 V. The transconductance g_m is 26 mS/mm at 2.5 V of gate bias (at which point the gate is drawing a current of about 750 μA). The value of g_m is lower than that obtained on previously fabricated fully implanted p-column[2] and conventional[3] InP JFETs. This is partly attributed to the high series gate resistance of the thick p^+-AlInAs layer and interfacial defects.
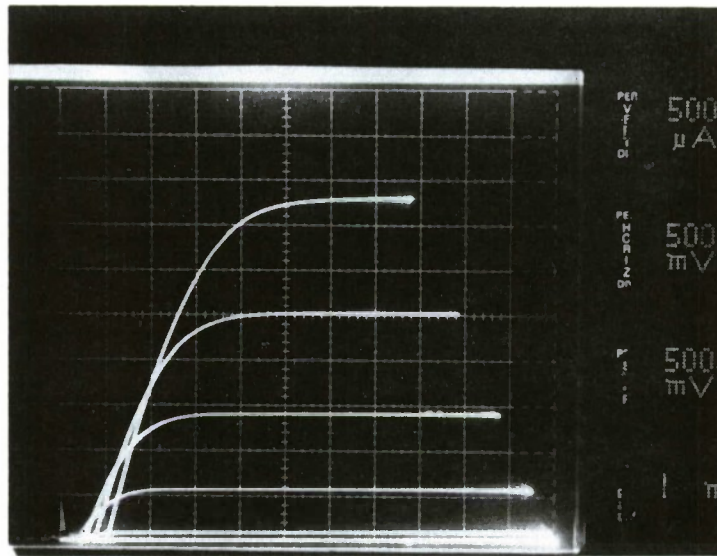
Figure 1-2.   Typical enhancement-mode I-V characteristics of a 1.0-μm-gate-length p^+-AlInAs/InP JFET.

2

Based on these initial results, it should be possible to fabricate depletion-mode devices by growing a thin undoped AlInAs buffer layer as a diffusion barrier prior to growth of the p[+] layer to reduce the depth of the p-n junction. A reduction of the p[+]-AlInAs thickness should also reduce the amount of Be indiffusion by decreasing the growth time, and at the same time should reduce the gate series resistance.

J.D. Woodhouse   M.J. Manfra
J.P. Donnelly   R.J. Bailey

1.2. EXPERIMENTAL EVALUATION OF THE PHOTOREFRACTIVE EFFECT IN Ti-INDIFFUSED LiNbO₃ WAVEGUIDES

The photorefractive effect refers to a mechanism whereby refractive index changes are caused by light. This effect has some applications, but it is a problem in most integrated optical devices when it occurs. The photorefractive effect in $LiNbO_3$ (References 4 and 5) is caused by ionization of impurities, primarily Fe^{2+}. Photogenerated electrons move in the crystal and change the internal electric fields, thus inducing index changes through the electrooptic effect. There are two basic aspects of the photorefractive effect, the photovoltaic and photoconductive effects. In the photovoltaic effect, photogenerated electrons drift in the +z direction because of a mechanism related to crystal anisotropy. This effect can occur in the absence of any applied electrical field. The charge builds up where the intensity changes, e.g., at the edge of a uniformly illuminated region.[6] The charge continues to build up until the space-charge field is large enough to balance the anisotropy-induced drift. Index changes arising from the photovoltaic effect can cause other effects, such as increased insertion loss,[7] polarization mode conversion,[8] and increased scattering.[9] In the photoconductive effect, charge moves in the direction of an externally applied field. This charge can build up and partially cancel an applied dc field.

The purpose of these experiments was to measure the two basic photorefractive effects (photovoltaic and photoconductive) in single-mode titanium-indiffused waveguides in the wavelength range 0.85 to 1.3 μm, which corresponds to the range used for most devices. We used an integrated-optical Mach-Zehnder interferometer to make sensitive measurements of the index changes caused by the photorefractive effect[10] (see Figure 1-3). The optical power in the two arms was made unequal by putting a chrome absorber on one arm (transmission was typically 5 percent). This produced much greater photovoltaic index changes in the brighter arm, thereby generating a phase difference between the light traveling through the two different arms. Electrodes on one arm were used to evaluate the photoconductive effect by applying a dc voltage. No voltage was applied in the photovoltaic measurements. The phase difference between arms was sensed by applying an ac signal and measuring the harmonics on a spectrum analyzer. The phase could be measured accurately by means of the ratio of the 1st and 2nd harmonics; this ratio is independent of the input optical power level. Because of the long arm length (50 mm) and accurate phase measurement (typically 1°), this experiment could sense small index changes (on the order of 10^{-7}).
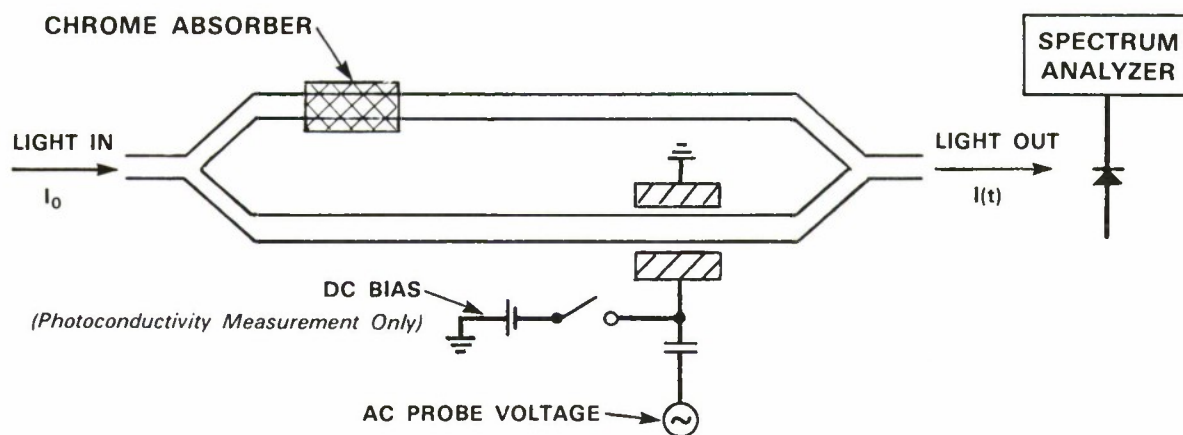
Figure 1-3. Method for measuring photorefractive effect.

The waveguides were all formed by titanium-indiffusion at 1000° or 1050°C with oxygen flowing through a bubbler filled to a depth of 15 cm with 25°C water. The electrodes were gold with a silicon dioxide buffer layer underneath; the SiO_2 layer was etched away everywhere except directly underneath the gold to avoid any effects due to conductivity through the oxide. All crystals were x-cut and the TE mode was always used, so light was polarized along the z-axis in the y-propagating case, and along the y-axis in the z-propagating case. The photovoltaic effect was measured by illuminating the devices with a constant optical intensity for up to 70 h, and observing the phase difference (which indicates the index difference) between interferometer arms during this time.

The index change was seen to have approximately an exponential dependence on time: $\Delta n = \Delta n_{sat} - (\Delta n_{sat} - \Delta n_{initial}) \exp [-t/\tau]$. At all power levels that produced a detectable index change, all the devices showed this time dependence, but with time constants τ and saturation index changes Δn_{sat} that depended on wavelength, propagation direction, and power level. A typical result is shown in Figure 1-4. Table 1-1 shows the saturation index changes and time constants seen at the highest optical power levels we were able to use. The index changes were smaller and the time constants longer at lower power levels. (These are all single-mode waveguides; typical cross-sectional area is about 6 μm^2 at 0.85 μm.) As expected, y-propagating waveguides had substantial index changes at 0.85 μm and much reduced (if any) changes at 1.3 μm. There is measurable index change in z-propagating waveguides, even at the 1.06-μm wavelength. This change is not predicted by the simplest explanation of charge separation along only the z-axis.[7] The index change is much smaller than that seen in y-propagating waveguides, and the relative size of the index change is much less than the ratio of electrooptic coefficients r_{22}/r_{33}. This implies that much smaller fields are induced in the y direction. This indicates that the primary photovoltaic effect is indeed charge separation along the z-axis. The cause of the small effect seen in z-propagating waveguides is unclear. It might be caused by the waveguides being slightly out of parallel with the z-axis.

4
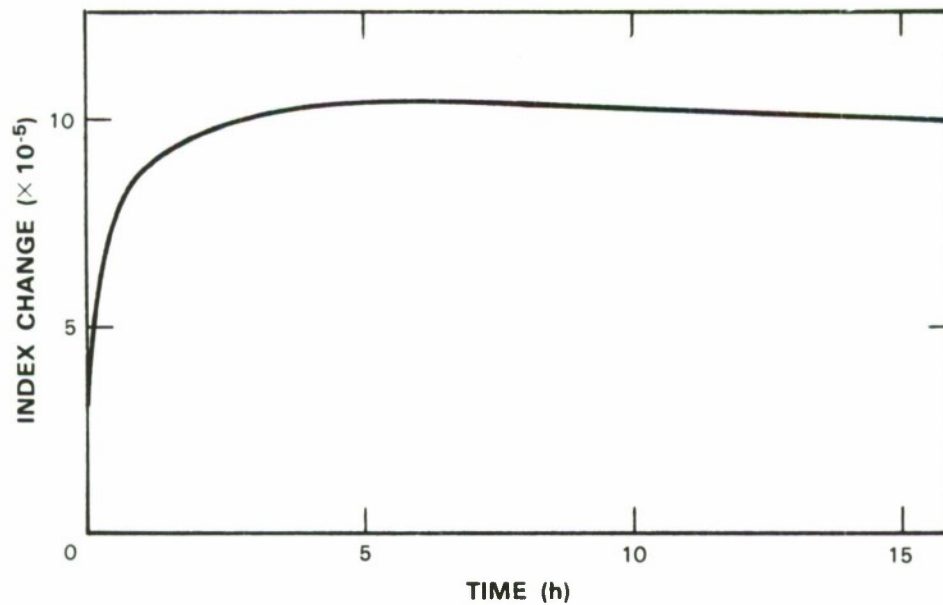
Figure 1-4. Photovoltaic effect. λ = 0.85 μm, y-propagating, 11 μW in waveguide.

TABLE 1-1				
Photovoltaic Index Changes **(at Highest Power Levels Used)**				
Wavelength (μm)	Propagation Direction	Optical Power (μW)	Index Change	Time Constant (s)
0.85	y	11	1.04×10^{-4}	4,500
1.3	y	400	$\leqslant 1.2 \times 10^{-6}$	—
0.85	z	35	1.6×10^{-6}	18,000
1.06	z	8200	1.9×10^{-6}	850

5

On test devices, the photoconductive effect was measured after the photovoltaic measurement so that the photovoltaic effect had already saturated. The dc voltage was applied without changing the optical intensity, and the index change was monitored over several hours as in the photovoltaic measurement. In the photoconductive effect, there is an initial index change due to the applied field; this index change then decays (a typical result is shown in Figure 1-5). When the delay is fitted with a single exponential, the index change predicted for infinite time is not zero. Table 1-2 shows the percentage of index canceled and the time constants measured for the photoconductive effect at the highest optical powers used. The photoconductive effect is significant in both y- and z-propagating devices. The photoconductivities are somewhat lower in z-propagating material than in y-propagating at the same intensity and wavelength, but the difference is much smaller than the difference in the photovoltaic effect. This is expected since the electrons produced by photoionization tend to drift in any direction in response to an externally applied field. The amount of field and index cancellation depends upon the amount of Fe^{2+} present relative to the charge needed to cancel the field, and upon the leakage current through the external bias circuit. These factors, and hence the percentage of index canceled, are much more subject to variation from device to device than the magnitude of the photoconductivity; we have included these percentages here primarily to show how serious a problem the photoconductive effect can be.

We can draw several conclusions from this work. (1) In the cases examined, the photorefractive effect is fairly simple, basically a monotonic index change that eventually saturates. (2) z-propagating waveguides are much less sensitive to the photovoltaic effect than y-propagating waveguides, but photovoltaic effects do occur. (3) The photoconductive effect can be significant in both y- and z-propagating waveguides. (4) Photorefractive effects are smaller at long wavelengths (>1 μm), but they can occur when the power is large enough (see also Reference 11). Finally, it should be noted that we have only evaluated a few different crystals and one waveguide fabrication technique, and that the magnitude of photorefractive effects may be different for crystals from different suppliers or for different waveguide fabrication techniques.

G.E. Betts

1.3. LARGE-NUMERICAL-APERTURE InP LENSLETS BY MASS TRANSPORT

There has been considerable interest in large-numerical-aperture lenslets[12-18] (approximately 100 μm in diameter) which can be used to greatly reduce the semiconductor-laser beam divergence and to help couple the laser light into an optical fiber or external cavity.[16,19,20] Lenslet arrays can also be employed to improve the poor fill factors of semiconductor laser arrays.[16] Further applications in optical interconnections for VLSI systems[21] or in "stacked planar optics"[22] have also been considered. In the present work, we explore the use of a mass-transport technique[23,24] in the fabrication of refractive lenslets in InP. Since the mass transport works toward a minimization of the surface energy, transport can smooth out an etched mesa structure to the shape of a lens, as shown in Figure 1-6.
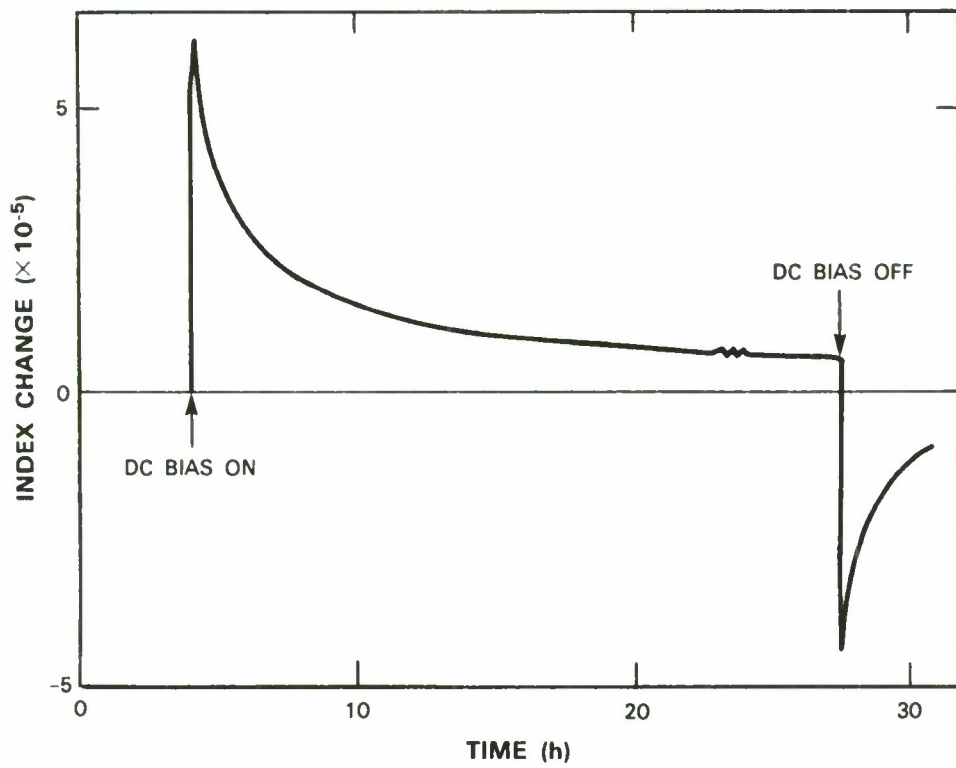
Figure 1-5.   Photoconductive effect. λ = 0.85 μm, z-propagating, 29 μW in waveguide, 22-V dc bias.

TABLE 1-2
Photoconductive Effect **(at Highest Power Levels Used)**

Wavelength (μm)	Propagation Direction	Optical Power (μW)	Percent of Bias Field Canceled	Time Constant (s)	Conductivity (from Time Constant)* (Ω-m)$^{-1}$
0.85	y	14	56	8,600	3 $\times$ 10^{-14}
1.3	y	300	<5	—	—
0.85	z	29	92	27,000	1.4 $\times$ 10^{-14}
1.06	z	4400	52	4,200	9 $\times$ 10^{-14}

* $\sigma = \dfrac{\epsilon_0 \epsilon}{\tau}$ [dark conductivity was $\approx$1.5 $\times$ 10^{-15} (Ω-m)$^{-1}$]

87265-5

7

(a)

(b)

(c)

87265-6
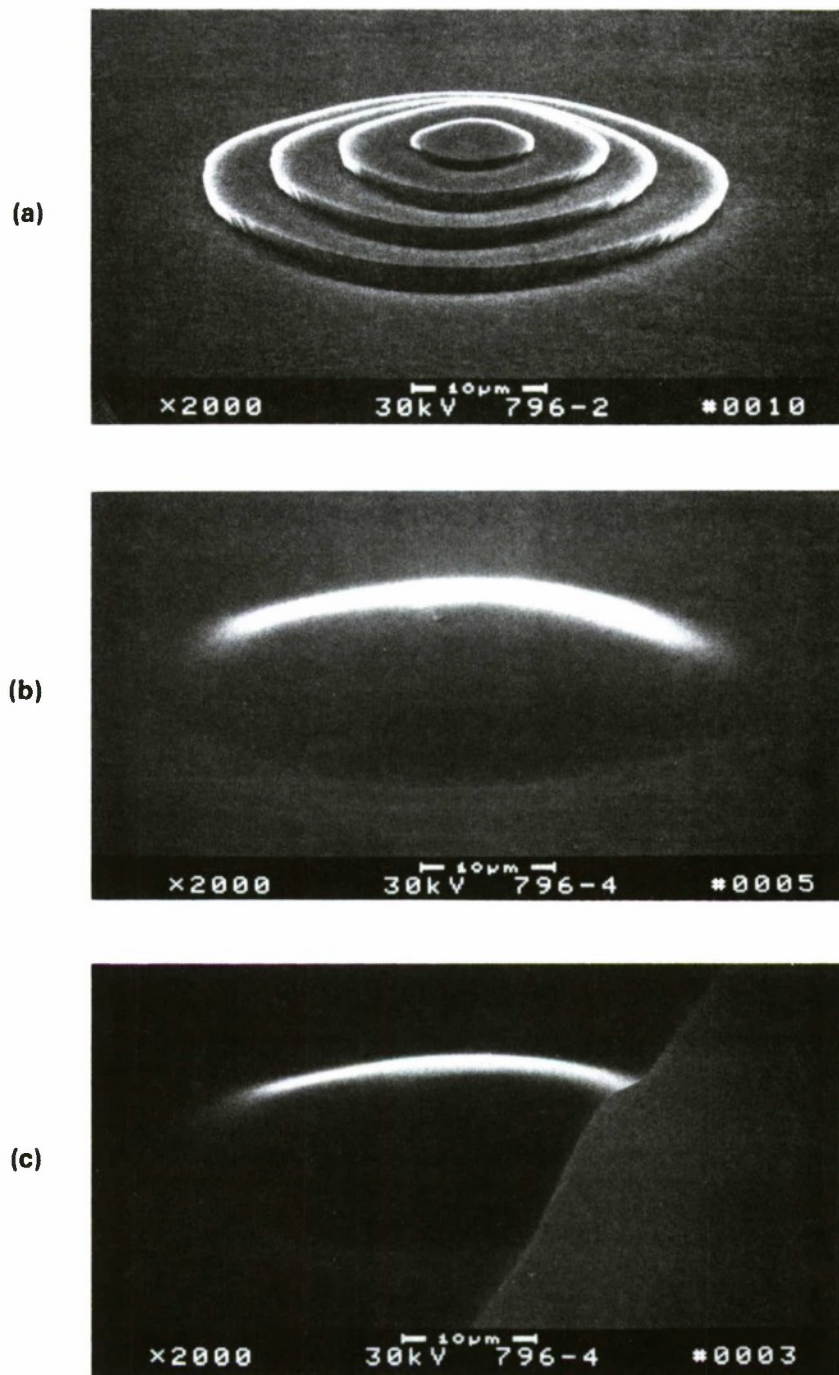
Figure 1-6.   SEM photographs showing the fabrication of a lenslet in InP: (a) multilayer mesa structure formed by chemical etching; (b) smooth lens surface obtained after mass transport. This lenslet has a diameter of 45 μm, a thickness of 4.0 μm, and a focal length of approximately 20 μm (in air and for 1.3-μm wavelength). The cleaved facet in (c) shows a lens cross section.

The fabrication procedure is illustrated in Figure 1-6. First, multilevel mesa structures which are nearly cylindrically symmetric are formed in a (100) InP substrate by repeated applications of photolithography and chemical etching. The etching step heights are designed on the assumption that mass is conserved during mass transport. The step heights are chosen to yield a desired lens profile, as illustrated in Figure 1-7(a). Then, the mass transport is carried out in H_2 and PH_3 flow at temperatures between 800° and 850°C for 2 to 10 h.

A very smooth lens surface has been obtained after mass transport, as shown in the SEM photograph in Figure 1-6(b). The cleaved facet in Figure 1-6(c) shows that a smooth lens profile has been obtained.

To accurately control the lens profiles, care has been exercised to achieve precise lithographic mask realignments and consistent chemical etching rate. The misalignment observed in earlier wafers [see Figure 1-6(a)] has been greatly reduced. The solid curve in Figure 1-7(b) shows a stylus surface profiling of an experimentally obtained lens profile after mass transport. After correcting for the broadening due to the size of the stylus (a spherical tip of 12.5-μm radius), the profile indeed closely approximates that of an ideal lens, shown as the dashed curve in Figure 1-7(b).

To optically test the lenslets, another wafer has been fabricated with lenslets similar to that in Figure 1-7(b) but with a longer focal length f of approximately 80 μm. [The lens thickness is approximately 3.4 μm and is smaller than that in Figure 1-7(b).] The back side of the wafer is polished and coated with a pyrolytically deposited SiO_2 layer of approximately 0.22-μm thickness (an approximate antireflection coating). A similar SiO_2 coating is also applied to the lenslets on the front side. The rest of the front surface is then coated with sputtered Au of an estimated 100- to 300-Å thickness. As shown in the inset in Figure 1-8, a GaInAsP/InP buried-heterostructure (BH) laser[24] of 1.3-μm wavelength is then positioned at the focal point in front of a lenslet for a minimum divergence of the laser light emerging from the back side of the wafer. The experimental result in Figure 1-8 shows a central lobe of 1.4° angular width and a series of fringes similar to a Fraunhofer diffraction pattern[25] but with somewhat irregular and higher intensities. The angular positions of the minima are nevertheless in good agreement with those of the Fraunhofer diffraction pattern of a 60-μm-diam. aperture, which is somewhat smaller than the measured lenslet diameter of approximately 67 μm. A better agreement is obtained if the peripheral region with curvatures deviating from the ideal lens profile is discounted [cf. Figure 1-7(b)]. Deviations from the ideal diffraction pattern can also be caused by lens imperfections (see below) and the fact that the lenslet is not fully uniformly illuminated by the BH laser.

One major imperfection of the present lenslets is a deviation from a complete cylindrical symmetry resulting from the anisotropic (crystallographic dependent) undercutting of the wet chemical etching.[26] In the wafer of Figure 1-8, the mesa diameter in the directions of the maximum undercutting (which are at 45° angles with the cleaved facets) is reduced by approximately 5 percent, and a corresponding variation in focal length is expected. This problem can be corrected either by more sophisticated lithographic techniques or by using ion-beam etching.[26]

9

(a)

LENS

ETCHED MESA

V_1
V'_1
V_2
V'_2
V_3
V'_3

ΔR

InP

87265-7

(b)

WAFER 797, #2-3

STYLUS SURFACE PROFILE
(Stylus Radius = 12.5 μm)

IDEAL
f = 45 μm

HEIGHT (μm)

POSITION (μm)

87265-47
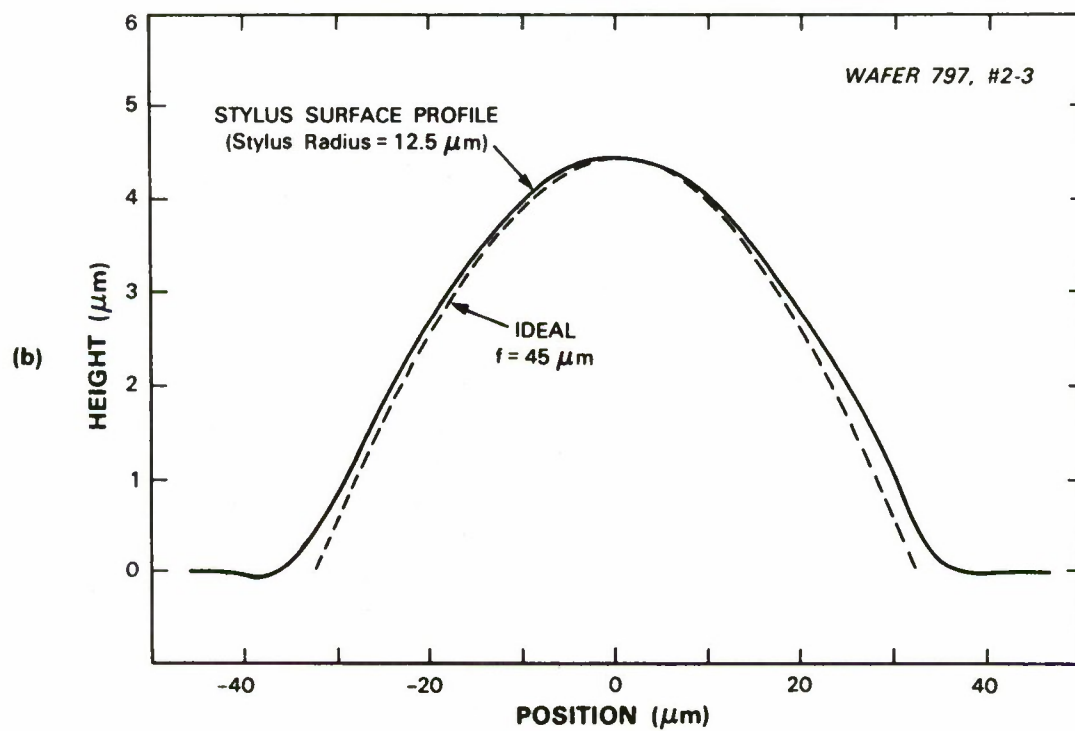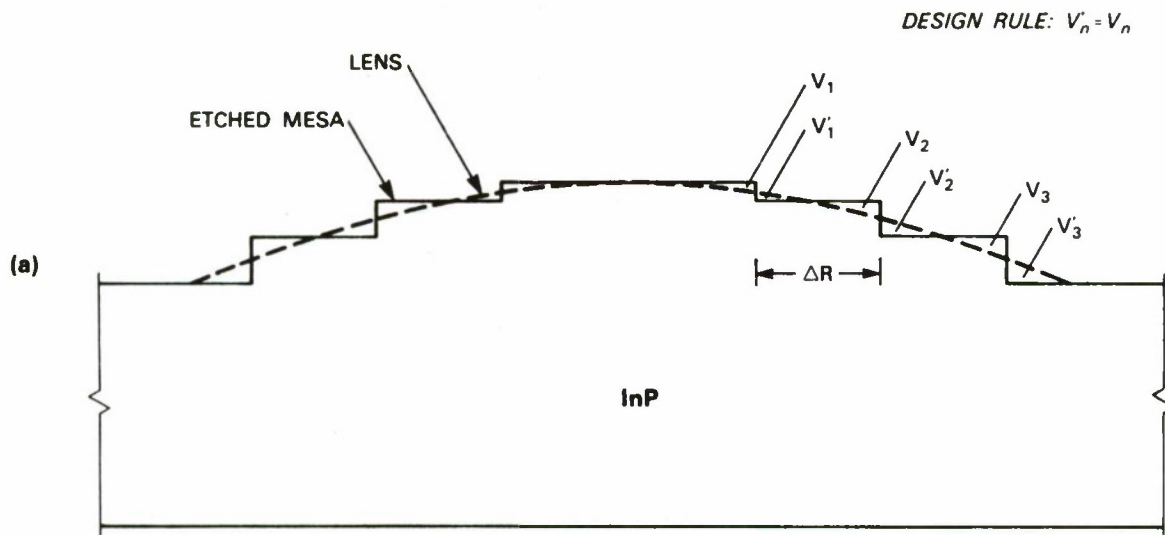
Figure 1-7. (a) Design of the multilevel mesa structure for the formation of a desired lens profile after mass transport. V_n is the volume of transported InP in the various regions. (b) A lens profile obtained experimentally.
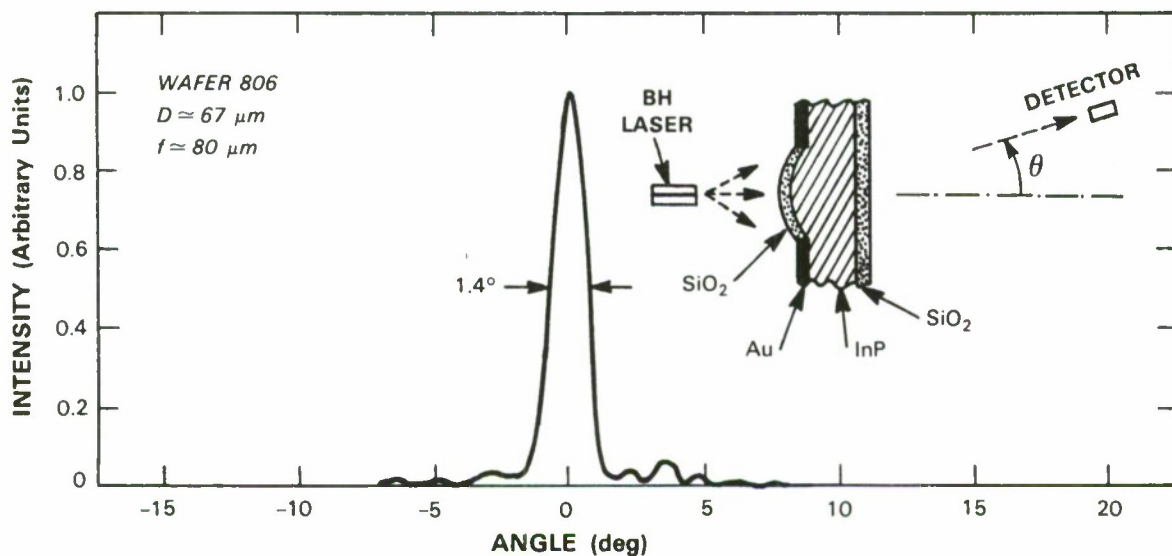
Figure 1-8. A far-field pattern obtained by placing a GaInAsP/InP BH laser at the focal point of a mass-transported lenslet. Note that the narrow central lobe of 1.4° angular width is nearly diffraction limited.

In conclusion, an initial demonstration has been made of mass transport as a promising technique in forming refractive lenslets. A very smooth lens surface has been achieved. Accurate control of the lens profile has been demonstrated and has resulted in a nearly diffraction-limited beam collimation. More work is needed to minimize the imperfections and to fabricate larger diameter lenslets.

Z.L. Liau
V. Diadiuk
J.N. Walpole

1.4. A SIMPLE FURNACE SYSTEM FOR HIGH-TEMPERATURE MASS-TRANSPORT EXPERIMENTS

Recent development of the mass-transport technique has resulted in novel device structures for GaInAsP/InP integrated optoelectronics.[23,24,27-31] Extension of the technique to the previously unexplored high-temperature regimes (>750°C) may yield yet newer device fabrication capabilities and provide deeper insights into the mass-transport phenomenon.

The high-temperature experiments, however, require higher phosphorus vapor pressure in order to totally suppress the InP decomposition. This results in excess phosphorus accumulation in the system which can lead to smoke, fire, and contamination during the sample unloading. To avoid the problem, we describe in this work a simple furnace-system design which has been successfully implemented and used for mass-transport experiments up to 910°C.

11
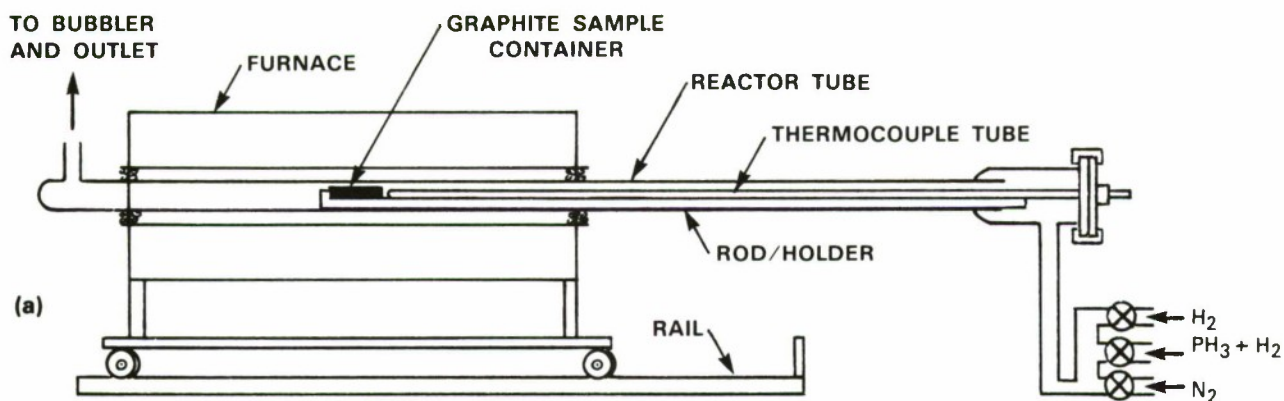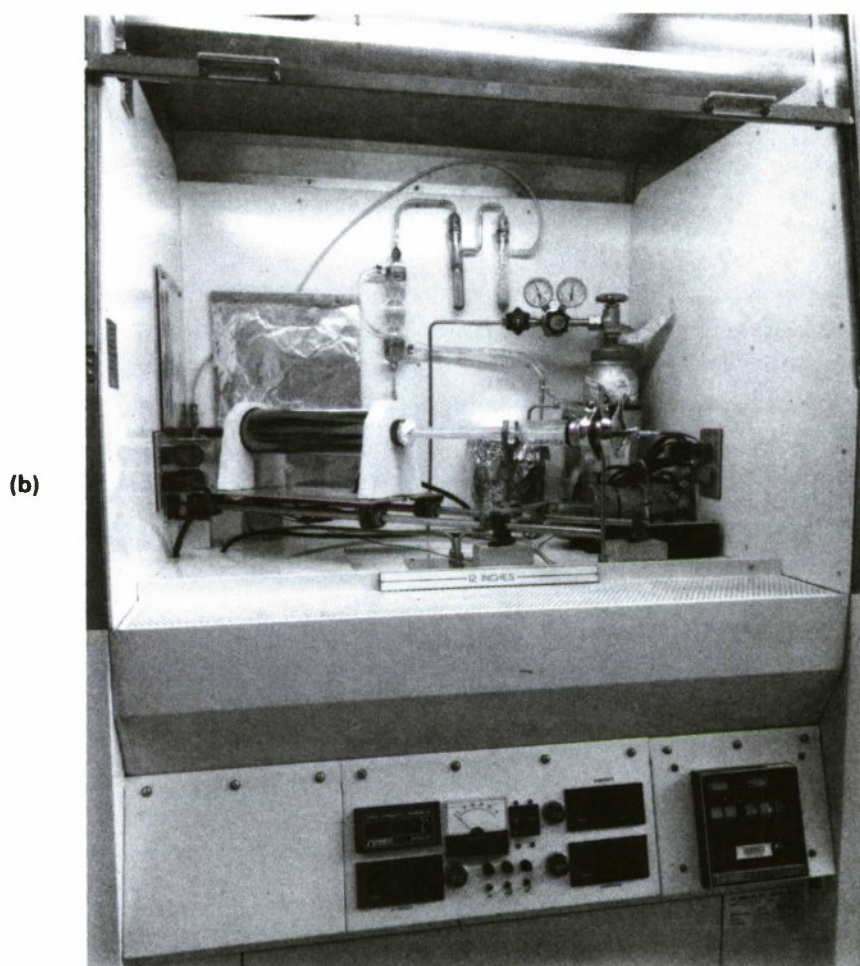
Figure 1-9. Schematic diagram (a) and photograph (b) of the present system. Note that the photograph shows phosphorus accumulation only in the rear end of the system.

The basic concept of the present design is to minimize the amount of phosphorus and to avoid its contact with room air during sample unloading. These goals are achieved in a simple way by using a reactor tube with a minimum diameter (just large enough for the present wafer size) but with an extra length between the furnace and the front end (where sample loading takes place), as illustrated in Figure 1-9. The thermocouple tube and the rod/holder further reduce the volume, increase the gas flux in the front part of the reactor tube, and therefore decrease the phosphorus accumulation there. This design has indeed resulted in a total elimination of the phosphorus deposition in the front end, in sharp contrast with our earlier, unoptimized design. Only a small section (less than 5 cm in length, depending on the gas flow and the temperature) adjacent to the furnace showed some phosphorus deposition. Even this is totally re-evaporated and purged to the rear end (after the mass transport is completed) by sliding the furnace forward (after it has been cooled to a lower temperature) and by greatly increasing the H_2 flow. Thus, all the phosphorus is deposited deep in the rear end of the long, narrow tube and its contact with room air during sample unloading is therefore minimized. To further prevent the room air from entering the tube, N_2 is flushed at a high rate when the system is open for sample loading and unloading.

Mass-transport experiments up to 910°C have been successfully carried out in this system without the phosphorus hazard. Figure 1-10(a-d) shows top views of an etched multilevel mesa structure on an InP substrate before and after mass transport at approximately 880°C for 18 h. Note that the mass transport has smoothed the 120-μm-diam. mesa structure (with a maximum height of approximately 6.0 μm) to form a lens. Indeed, good-quality InP lenslet arrays have been fabricated this way and will be reported elsewhere.[31] This is made possible by the high-temperature mass transport which is capable of smoothing large mesa structures. The present high temperature was limited by the phosphine concentration used (approximately 5 percent), because severe InP decomposition was observed above 900°C. Further improvement of the system should also include a phosphorus filter or absorber in the rear end.

In conclusion, a simple furnace system has been proposed and successfully implemented to avoid the phosphorus problem in high-temperature mass-transport experiments.

Z.L. Liau
D.E. Mull
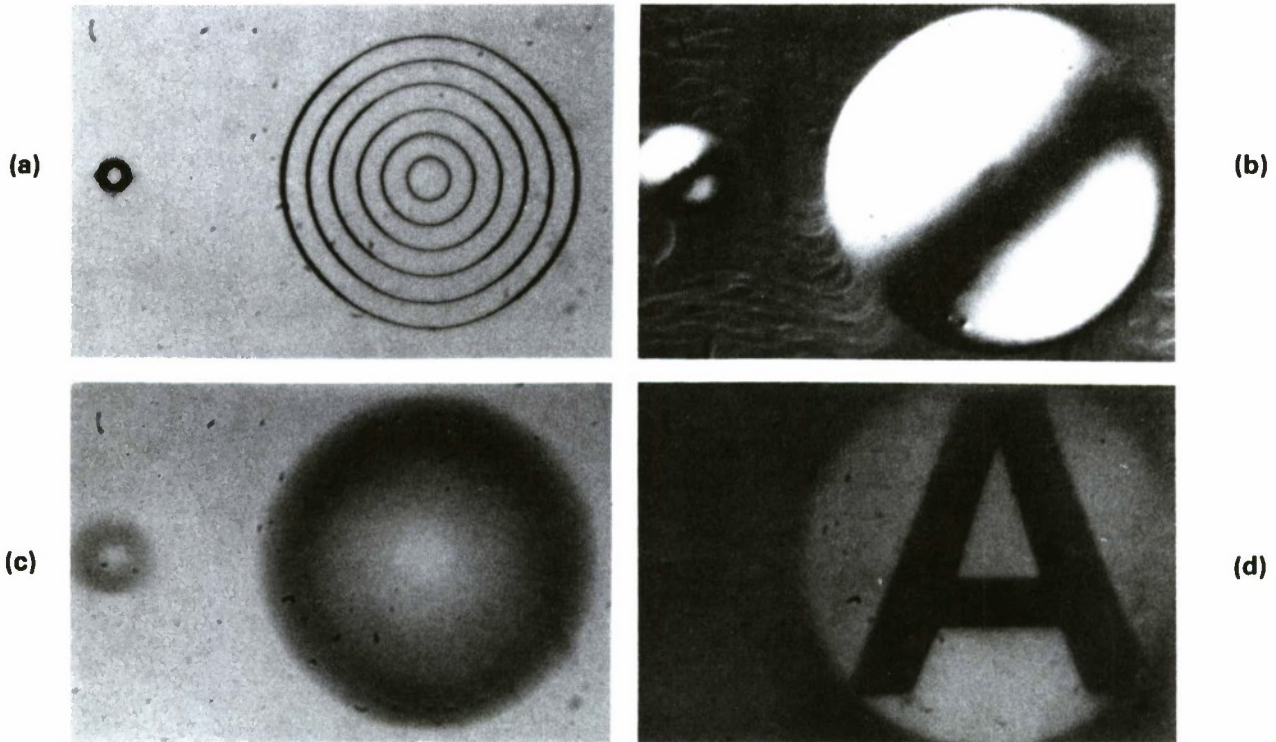
Figure 1-10. Optical micrographs of the top views of chemically etched multilevel mesa structures (a) before, and (b), (c), and (d) after mass transport at 880°C. Note that (a) and (b) are ordinary micrographs taken under nearly identical conditions, while interference contrast has been used in (c). The maximum diameter in (a) is 120 μm. Part (d) is an image formed by the reflected light, i.e., by using the lens surface as a spherical mirror.

REFERENCES

1. J.D. Oberstar, B.G. Streetman, J.E. Baker, and P. Williams, J. Electrochem. Soc. **129**, 1312 (1982).

2. J.D. Woodhouse and J.P. Donnelly, IEEE Electron Device Lett. **EDL-7**, 387 (1986).

3. J.B. Boos, H.B. Dietrich, T.H. Weng, K.J. Sleger, S.C. Binari, and R.L. Henry, IEEE Electron Device Lett. **EDL-3**, 256 (1982).

4. A.M. Glass, Opt. Eng. **17**, 470 (1978).

5. A.M. Glass, I.P. Kaminow, A.A. Ballman, and D.H. Olson, Appl. Opt. **19**, 276 (1980).

6. L.B. Schein, P.J. Cressman, and F.M. Tesche, J. Appl. Phys. **48**, 4844 (1977).

7. R.L. Holman, Proc. SPIE **408**, 14 (1983).

8. J.F. Lam and H.W. Yen, Appl. Phys. Lett. **45**, 1172 (1984).

9. Y. Handa, M. Miyawaki, and S. Ogura, Proc. SPIE **460**, 101 (1984).

10. R.A. Becker and R.C. Williamson, Appl. Phys. Lett. **47**, 1024 (1985), DTIC AD-A164342.

11. G.T. Harvey, G. Astfalk, A.Y. Feldblum, and B. Kassahun, IEEE J. Quantum Electron. **QE-22**, 939 (1986).

12. O. Wada, S. Yamakoshi, M. Abe, Y. Nishitani, and T. Sakurai, IEEE J. Quantum Electron. **QE-17**, 174 (1981).

13. M. Oikawa and K. Iga, Appl. Opt. **21**, 1052 (1982).

14. K. Tatsumi, T. Saheki, T. Takei, and K. Nukui, Appl. Opt. **23**, 1742 (1984).

15. O. Wada, J. Electrochem. Soc. **131**, 2373 (1984).

16. J.R. Leger, G.J. Swanson, and M. Holz, *Topical Meeting on Semiconductor Lasers, Technical Digest, 1987, Volume 6* (Optical Society of America, Washington, DC, 1987), pp. 80-83.

17. V. Diadiuk, J.N. Walpole, and Z.L. Liau, *Topical Meeting on Semiconductor Lasers, Technical Digest, 1987, Volume 6* (Optical Society of America, Washington, DC, 1987), pp. 91-94.

18. T. Shiono, K. Setsune, O. Yamazaki, and K. Wasa, Appl. Opt. **26**, 587 (1987).

19. R.H. Rediker, R.P. Schloss, and L.J. Van Ruyven, Appl. Phys. Lett. **46**, 133 (1985).

20. J.R. Leger, G.J. Swanson, and W.B. Veldkamp, Appl. Phys. Lett. **48**, 888 (1986), DTIC AD-A167573.

21. See, for example, J.W. Goodman, F.J. Leonberger, S.Y. Kung, and R.A. Athale, Proc. IEEE **72**, 850 (1984).

22. K. Iga, M. Oikawa, S. Misawa, J. Banno, and Y. Kokubun, Appl. Opt. **21**, 3456 (1982).

23. Z.L. Liau and J.N. Walpole, Appl. Phys. Lett. **46**, 115 (1985), DTIC AD-A151425.

24. Z.L. Liau, J.N. Walpole, and D.Z. Tsang, IEEE J. Quantum Electron. **QE-20**, 855 (1984), DTIC AD-A149328.

25. See, for example, M. Born and E. Wolf, *Principles of Optics*, 5th edition (Pergamon Press, London, 1959), pp. 394-397.

26. See, for example, L.A. Coldren, K. Furuya, and B.I. Miller, J. Electrochem. Soc. **130**, 1918 (1983).

27. Z.L. Liau and J.N. Walpole, Appl. Phys. Lett. **40**, 568 (1982), DTIC AD-A121779.

28. Z.L. Liau, J.N. Walpole, and D.Z. Tsang, Appl. Phys. Lett. **44**, 945 (1984), DTIC AD-A147996.

29. Z.L. Liau, D.C. Flanders, J.N. Walpole, and N.L. DeMeo, Appl. Phys. Lett. **46**, 221 (1985), DTIC AD-A151583.

30. J.N. Walpole and Z.L. Liau, Appl. Phys. Lett. **48**, 1636 (1986).

31. Z.L. Liau, V. Diadiuk, and J.N. Walpole, unpublished.

2. QUANTUM ELECTRONICS

2.1. OPTICALLY INDUCED BIREFRINGENCE IN Ti:Al$_2$O$_3$

We have observed optically induced birefringence in Ti:Al$_2$O$_3$ at signal wavelengths of 632.8 and 790.7 nm during the course of small-signal gain measurements on a Ti:Al$_2$O$_3$ amplifier pumped with 532-nm radiation from a frequency-doubled Q-switched (10-ns pulses) Nd:YAG laser. The changes in intensity of the signal beam due to induced birefringence were found to decay with a time constant approximating the fluorescence lifetime of Ti^{3+} ions. We therefore attribute the induced birefringence to the Ti^{3+} excited state (^2E_g) population.

Figure 2-1 shows a schematic of the experimental setup used for the measurement of induced birefringence. The 532-nm pump beam propagates perpendicular to the c-axis of a Ti:Al$_2$O$_3$ crystal with its polarization vector parallel to the c-axis. The signal beam from a He-Ne (632.8 nm) or Ti:Al$_2$O$_3$ (790.7 nm) laser propagates almost collinearly ($\approx$1° angle) with the pump beam and is polarized at 45° with respect to the polarization of the pump beam, as shown in Figure 2-2. A sheet polarizer placed between the Ti:Al$_2$O$_3$ crystal and the silicon photodiode is used as an analyzer to observe the polarization-dependent changes in the intensity of the signal beam.
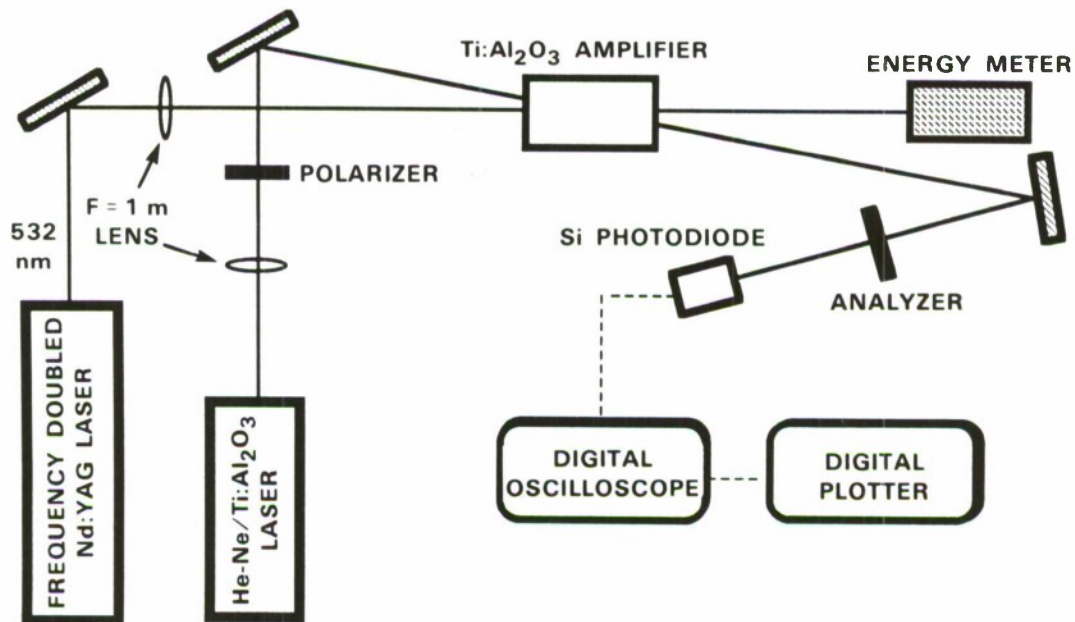
Figure 2-1.   Schematic of the experimental setup for the measurement of small-signal gain and optically induced birefringence.

17
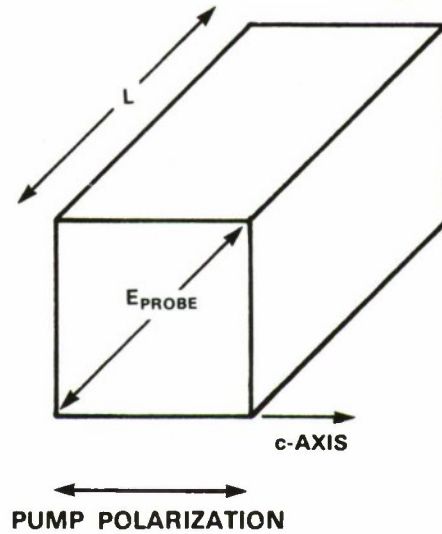
Figure 2-2. *Orientation of the pump- and signal-beam polarizations relative to the c-axis of the Ti:Al₂O₃ crystal.*

With the analyzer in the crossed orientation, which blocks the signal beam in the absence of the pump beam, the intensity of the signal beam at 632.8 nm exhibits gain following the pump pulse, as shown in Figure 2-3(a). In contrast, the intensity of the 632.8-nm beam with the analyzer in the parallel polarization exhibits a loss, as shown in Figure 2-3(b). These pump-induced changes $\Delta I_\perp$ and $\Delta I_\parallel$ in the crossed and parallel orientations, respectively, may be written as

$$\Delta I_\perp = I_0 \ e^{gL} \ \sin^2\left(\frac{\Delta\phi}{2}\right) \tag{2-1}$$

and

$$\Delta I_\parallel = -\Delta I_\perp + I_0 \ (e^{gL} - 1) \tag{2-2}$$

with

$$\Delta\phi = \left(\frac{2\pi}{\lambda_s}\right) \ L\delta\eta \tag{2-3}$$

where I_0 is the intensity of the signal beam for the parallel polarization in the absence of the pump beam, g is the time-dependent small-signal gain coefficient, L is the length of the crystal, $\Delta\phi$ is the time-dependent induced phase difference between the signal-beam polarization components parallel and perpendicular to the c-axis, λ_s is the vacuum wavelength of the signal beam, and $\delta\eta$ is the time-dependent induced birefringence.

18
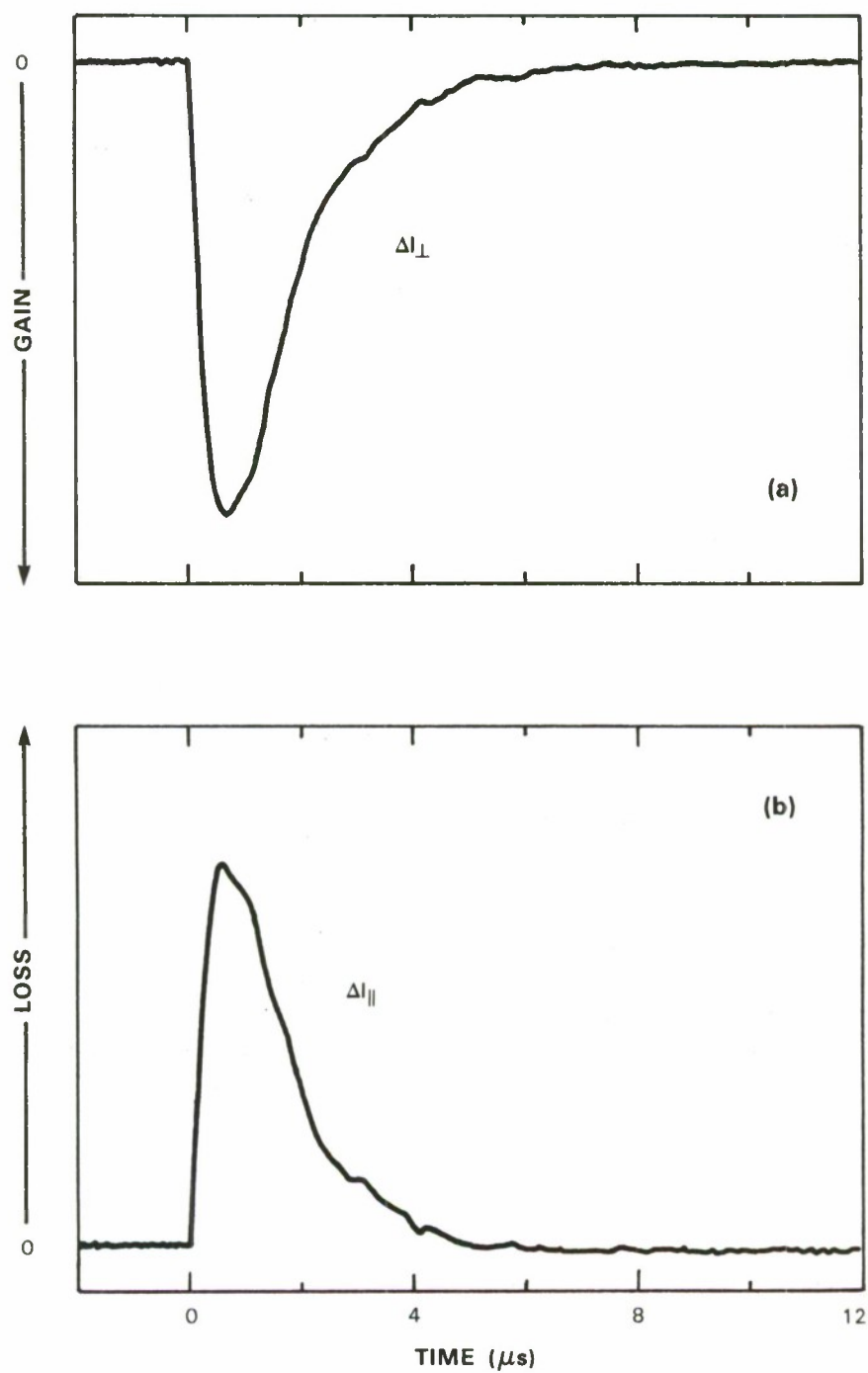
Figure 2-3. Temporal behavior of the birefringence-induced change in the signal-beam intensity at 632.8 nm in (a) the perpendicular polarization and (b) parallel polarization, showing gain and loss, respectively. The incident pump energy density was 3.5 J/cm².
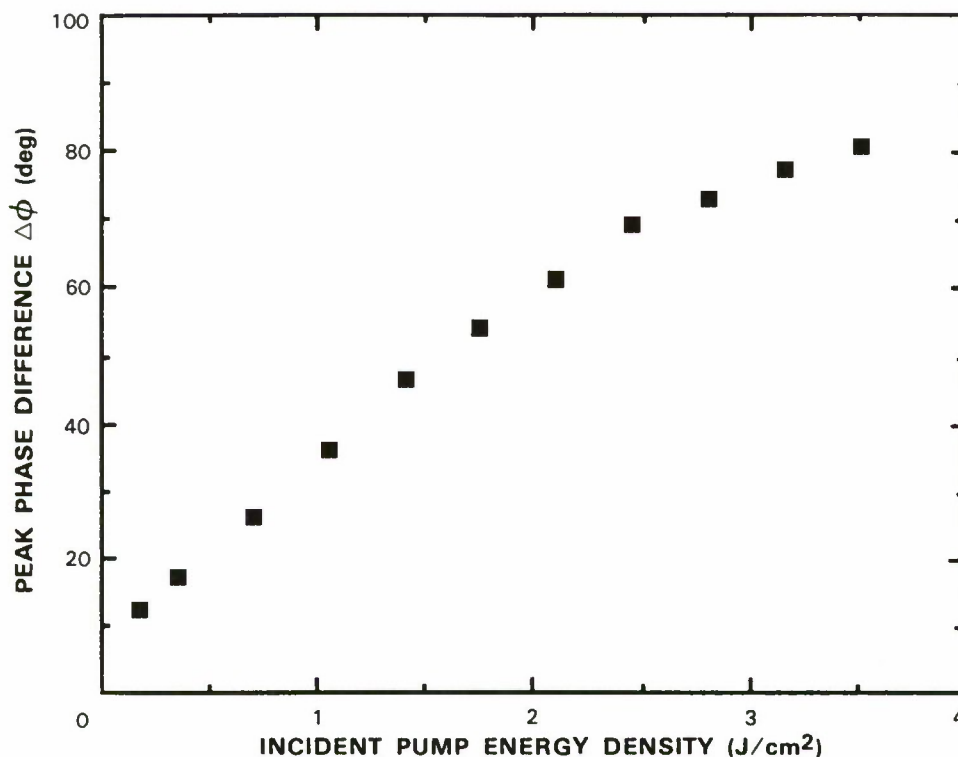
Figure 2-4. The peak value of the birefringence-induced phase difference Δφ (between the signal polarization components parallel and perpendicular to the c-axis) as a function of the incident pump energy density.

The observed variation of the peak value of $\Delta\phi$ with the pump energy density is shown in Figure 2-4 for the signal at 632.8 nm. Similar results have been obtained for the signal at 790.7 nm. It should be noted that the induced birefringence is not observed when the signal-beam polarization is exactly parallel or perpendicular to the c-axis. Therefore, the polarization of the input signal beam can be preserved by careful alignment with respect to the c-axis. This is necessary for achieving good isolation between different stages of an amplifier chain.

K.F. Wall   R.E. Fahey
R.L. Aggarwal   A.J. Strauss

2.2. SINGLE-FREQUENCY Ti:Al$_2$O$_3$ RING LASER

The ring cavity for the single-frequency TiAl$_2$O$_3$ laser is similar to one described in previous reports.[1] An argon-ion laser pumps a four-mirror ring containing the laser crystal, a Lyot filter, a thin etalon, and a Faraday rotator/compensator. The laser output is monitored by a power meter, wavemeter, and Fabry-Perot spectrum analyzer.

The Ti:Al$_2$O$_3$ crystal is pumped by all lines from a small argon-ion laser. The argon-ion laser beam is reflected twice for ease of alignment and to convert the vertical polarization to horizontal polarization. A 12.5-cm-focal-length lens focuses the beam into the laser cavity. The pump beam passes into the cavity through a 10-cm-radius dichroic mirror that is 90-percent transmitting in the blue-green and over 99.5-percent reflecting between 700 and 900 nm. The laser crystal is placed at the focus of the argon-ion laser beam, a position 5 cm from the input mirror.

A 0.5-mm-thick, uncoated etalon is sufficient to maintain single-frequency operation even at the highest power levels and allows access to every longitudinal mode of the cavity. By contrast, single-frequency dye lasers use two etalons with higher (20-percent) reflectivity coatings.[2] When the cavity is operated without an etalon, single-frequency operation can be obtained, but not every longitudinal mode can be accessed and the single-frequency operation is not maintained at higher powers.

The peak power output of the ring laser is 300 mW at 800 nm when it is pumped with 6.8 W from an argon-ion laser and a commercially available 3- to 5-percent output coupler is used. At this output wavelength, the ring laser threshold is 3.6 W of blue-green, giving a slope efficiency of 9 percent. The single-frequency laser tunes between 740 and 860 nm. When a different output coupler with 1- to 3-percent coupling is used, lasing occurs between 750 and 880 nm.

Figure 2-5 shows the frequency stability of the ring laser over a 10-s time period. The frequencies range over approximately 4 MHz in a few seconds. The rms frequency jitter obtained from these data is 1.6 MHz. This frequency jitter is probably a result of motion of a mirror of
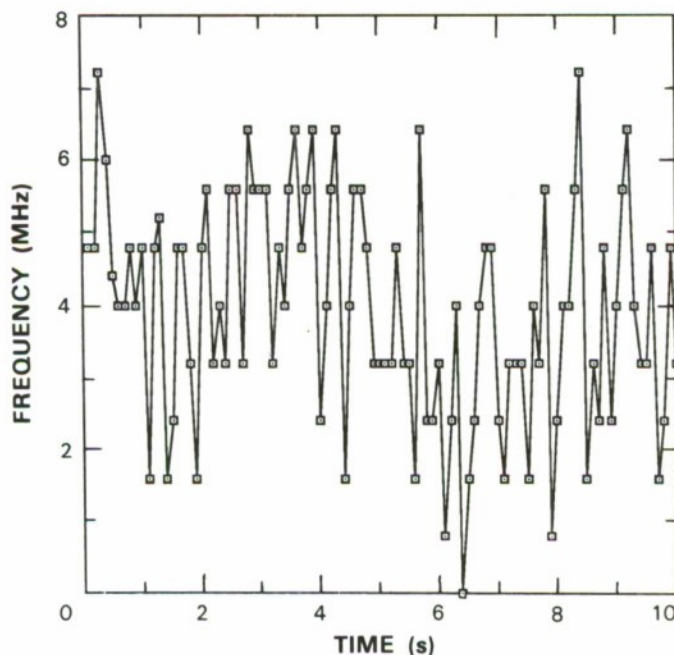
Figure 2-5. *Laser frequency vs time for a period of 10 s. The rms deviation from the mean frequency is 1.6 MHz.*

about 6 nm rms. Mirror motion can be decreased below this value, but not typically on optical breadboards such as in the present case. By comparison, a free-running dye laser has no better than approximately 10-MHz frequency jitter, with much of the jitter at high frequency caused by dye jet fluctuations. The linewidth for the dye laser can be reduced by frequency locking to an external cavity. No attempt was made to frequency lock the Ti:Al$_2$O$_3$ laser.

In addition to the jitter, the laser frequency shows a drift of 200 kHz/s. The drift of the laser frequency over 100 s amounts to a lengthening of the laser cavity by approximately 80 nm. The laser is mounted on a stainless-steel breadboard whose thermal expansion coefficient is 10^{-5}°C^{-1}. The expansion of 80 nm corresponds to a temperature change of 0.006°C. Mounting the laser on SuperInvar should reduce the laser frequency drift, because the thermal expansion coefficient is ten times smaller.

P.A. Schulz
S.K. McClung

2.3. SECOND-HARMONIC GENERATION FOR Ti:Al$_2$O$_3$ LASER PUMPING

Further frequency-doubling experiments with KTP crystals using the long-train Nd:YAG laser pulses were carried out. The laser macropulse consisted of a 100-μs-long train of 100-ps mode-locked pulses (micropulses) with 10-ns spacing, as previously described.[3,4] The KTP crystals used in these experiments were flux-grown, in contrast with previously investigated crystals which were grown by a hydrothermal technique. Two flux-grown crystals were studied, one $3 \times 3 \times 3$ mm in size and the other $3 \times 3 \times 10$ mm; they were antireflection coated at each end for both 1.06 and 0.53 μm.

The results obtained with the 10-mm-long crystal are shown in Figure 2-6. An average second-harmonic-generation (SHG) efficiency greater than 52 percent was obtained at an input power density below 20 MW/cm^2. Most of the departure from the initial slope is seen to be due to depletion of the fundamental frequency photons. The initial slope is 5.6-percent MW^{-1} cm^2; this is approximately 22 percent of the value calculated for this length crystal and is higher than has been observed with hydrothermally grown crystals.[4,5]

Damage in the form of a burn on the front surface of the crystal was obtained at an input power density of 20 MW/cm^2. This is significantly lower than the 35- to 50-MW/cm^2 damage thresholds which have been observed in hydrothermally grown crystals subjected to similar input pulses.[4,6] It is unknown at this time whether the lower damage threshold is characteristic of the material or the antireflection coating. In any event, at these damage threshold levels unacceptably large crystal apertures would be required for efficient frequency doubling at high input pulse powers.
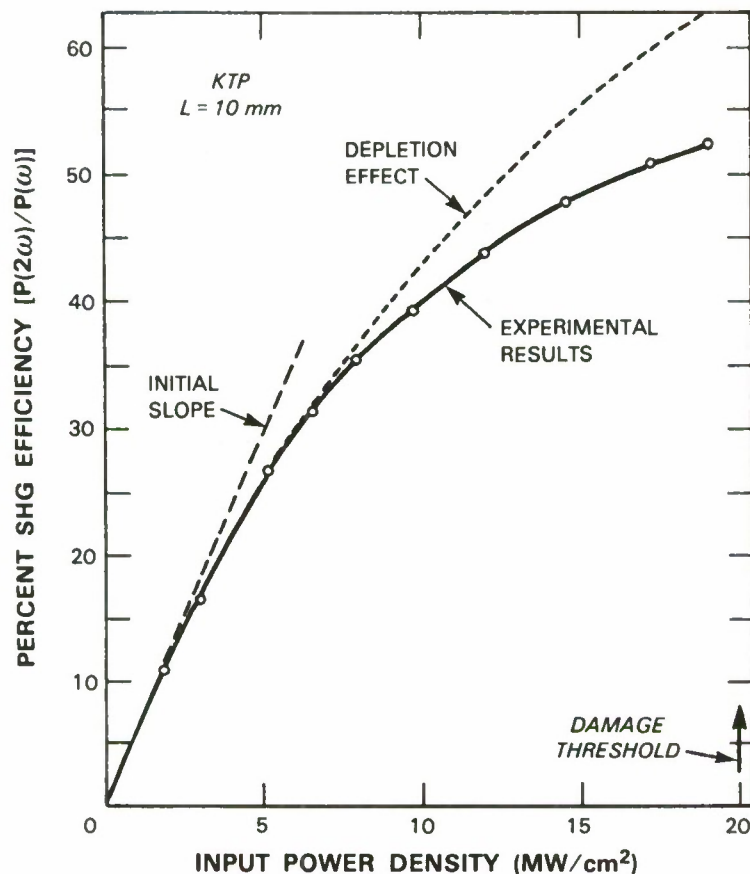
Figure 2-6. *Percentage SHG efficiency of a 10-mm-long KTP crystal as a function of input power density.*

Similar measurements carried out with the 3-mm-long crystal yielded 9-percent SHG efficiency at 18.5 MW/cm^2, and an experimental-to-calculated initial-slope ratio of approximately 27 percent was found. In view of its ability to achieve high SHG efficiency at relatively low input power density, KTP remains a material of considerable interest. However, it will be of practical value for high-average-power, high-peak-power application only if it can reasonably be grown in larger sizes than are presently available, and if it can withstand the input levels required for continuous operation at a high efficiency level (>50 percent) without sustaining optical damage.

The mode-locked Nd:YAG laser system described above was converted to Q-switched operation in order to study the relative merits of the latter for producing a high-average-power, high-peak-power fundamental frequency source for SHG. A Q-switched pulse energy output of ~1 J with a pulse length ~125 ns was obtained, as shown in Figure 2-7(a). It can be seen that significant mode beating is present. Attempts were made to reduce the number of modes by introducing a 1-mm aperture and by the addition of etalons in the laser oscillator cavity. While these

(a)
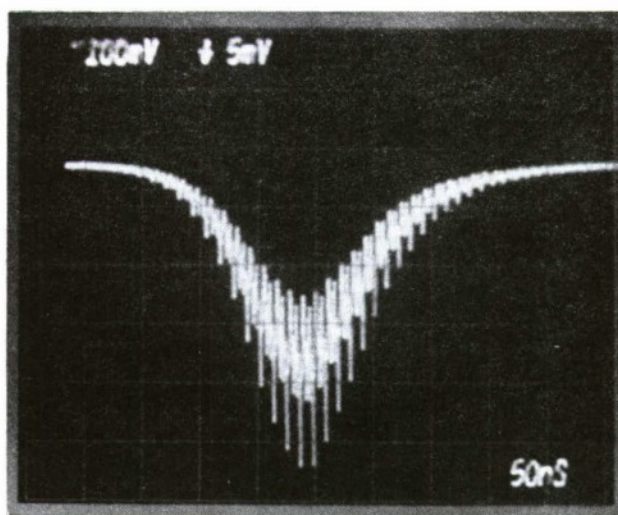
(b)
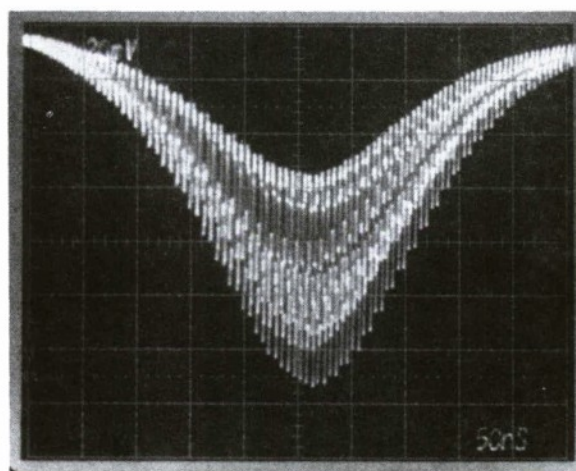
Figure 2-7.   Mode beating of Q-switched laser output, obtained using 0.05-ns detector and 1-GHz-bandwidth oscilloscope: (a) multiple transverse and multiple longitudinal modes; (b) single transverse and multiple longitudinal modes.

reduced the output to a single transverse mode, the presence of longitudinal modes led to a broadened pulse length and increased amplitude modulation, as seen in Figure 2-7(b).

The laser system was operated with the laser mode characteristics shown in Figure 2-7(a) to irradiate two $LiIO_3$ crystals, one $10 \times 10 \times 10$ mm, the other $10 \times 10 \times 15$ mm. These crystals had previously been irradiated at power densities up to 190 MW/cm^2 at a 10-Hz PRF without sustaining damage using the 100-μs mode-locked pulse train previously described.[3,4] In the Q-switched mode, at a 1.25-Hz PRF, serious bulk damage occurred at 66 and 53 MW/cm^2 in the 10- and 15-mm-long crystals, respectively. In view of these results, further attempts to use a Q-switched mode with this laser system were abandoned, and the laser was restored to mode-locked operation.

<div align="right">
N. Menyuk
K.F. Wall
</div>

2.4. Nd:YAG SUM-FREQUENCY GENERATION OF SODIUM RESONANCE RADIATION

We previously reported the generation of sodium resonance radiation by sum-frequency mixing the output radiation of two simultaneously Q-switched Nd:YAG lasers, one operating at 1.064-μm and the other operating at 1.319-μm (see Reference 7). We have recently achieved a much higher mixing efficiency by adjusting the two Q-switched pulse lengths to be more nearly equal. The 1.064-μm pulse was lengthened from 80 to 140 ns, and the 1.319-μm pulse was shortened from 250 to 200 ns. When the Nd:YAG lasers were operated at a 1-kHz repetition rate, the 1.064-μm laser had an average output power of 900 mW within a 1-GHz spectral range, the 1.319-μm laser had an average output power of 880 mW within a 1-GHz spectral range, and the 0.589-μm radiation had an average power of 395 mW within a 2-GHz spectral range. The sum-frequency mixing was accomplished in a 5-cm-long lithium niobate crystal which was held at a temperature of 224°C. At this temperature the lithium niobate has an index of refraction of 2.23, which results in a 14-percent reflection of the Nd:YAG and sum radiation at the uncoated crystal surfaces. The average intra-crystal frequency-mixing efficiency was 30 percent. Figure 2-8 shows the temporal behavior of the pulsed radiation which has passed through the summing crystal. The 1.064-μm pulse has a peak power depletion of about 30 percent, while the dip in the 1.319-μm pulse corresponds to a power depletion of about 40 percent.

The sodium D_2 transition saturates at an intensity of about 10 mW/cm^2 of single-frequency resonant radiation. Higher intensities of resonant radiation are increasingly less effective at exciting more sodium atoms. In order to optimize the efficiency of high-power resonant radiation, the frequency distribution of the radiation must be made to cover more of the Doppler-broadened absorption profile. By introducing an electrooptic phase modulator into the Nd:YAG laser cavity, the spectral output of the laser can be frequency modulated. When frequency modulated, the Nd:YAG laser will produce radiation on each longitudinal cavity mode over a wide frequency
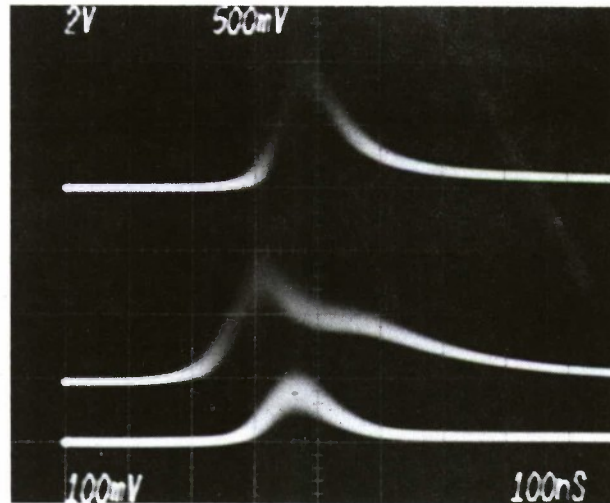
Figure 2-8.   Pulse shapes of the Nd:YAG and sum radiation after passing through the lithium niobate crystal. Upper trace: 1.064-μm pulse; middle trace: 1.319-μm pulse; lower trace: 0.589-μm pulse.

range. Figure 2-9 shows the spectral output of a 1.064-μm CW Nd:YAG laser at various levels of phase modulation. The frequency difference between adjacent cavity modes is 90.856 MHz. It is important to note that these spectral profiles are very stable in time and that all laser cavity modes participating in the frequency modulation are oscillating simultaneously. We have obtained stable operation of a frequency-modulated laser with as much as a 6-GHz spectral range. Unfortunately, the AD*P crystal which was used for frequency modulation had a high laser cavity insertion loss and reduced the operating power of the Nd:YAG laser from 10 W to 160 mW. We are planning to use a lithium niobate phase modulator which is much more transparent to the Nd:YAG radiation.

<div align="right">

T.H. Jeys   A.A. Brailove
D.K. Killinger   W.E. DeFeo

</div>

2.5. QUANTUM WELLS WITH CONTROLLABLE SPATIALLY DEPENDENT THICKNESSES

The ability to grow quantum well (QW) materials with controllable spatially dependent thicknesses adds design flexibility and increased utility to monolithic devices. Such devices could now include monolithically integrated lasers of different frequencies, tapered quantum well HEMTs, new waveguide devices, and improvements in spatial light modulators which use the QW excitonic Stark effect.

UNMODULATED MODULATED

POWER

FREQUENCY

POWER

FREQUENCY

MODULATION
INDEX

$\delta = X$

$\delta = 2X$

$\delta = 3X$

$\delta = 5X$

$\delta = 7X$

85099-1
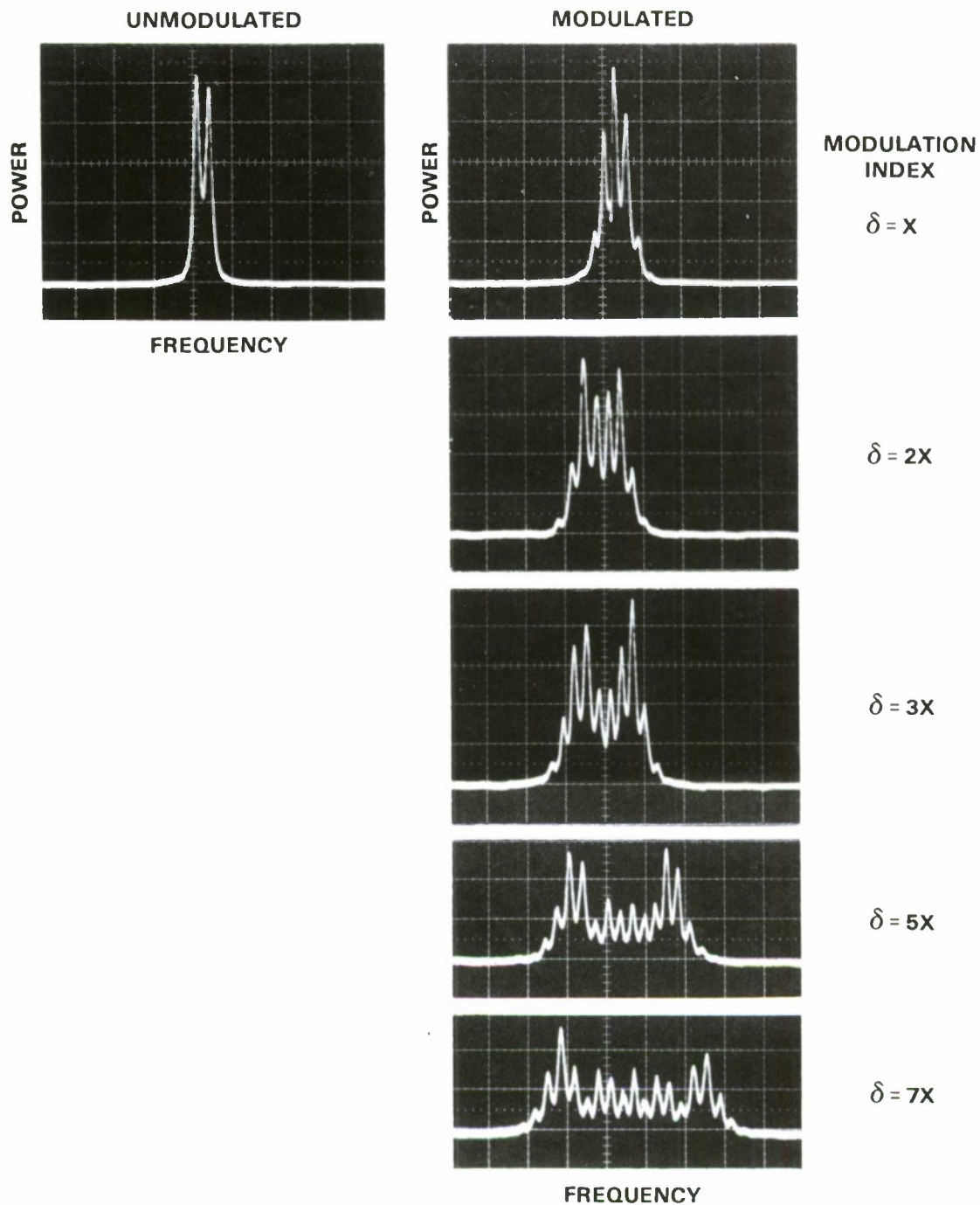
Figure 2-9. Spectral content of a frequency-modulated 1.064-μm Nd:YAG laser as measured by a Fabry-Perot spectrum analyzer. The spectra of the unmodulated laser is shown on the left and consists of two adjacent longitudinal cavity modes. The spectra of the modulated laser at various modulation levels δ are shown on the right. The laser cavity mode separation is 90.856 MHz.

27
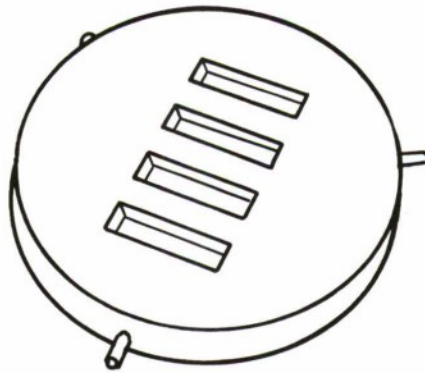
Figure 2-10. Sketch of the molybdenum substrate mounting block with milled slots used in this work.
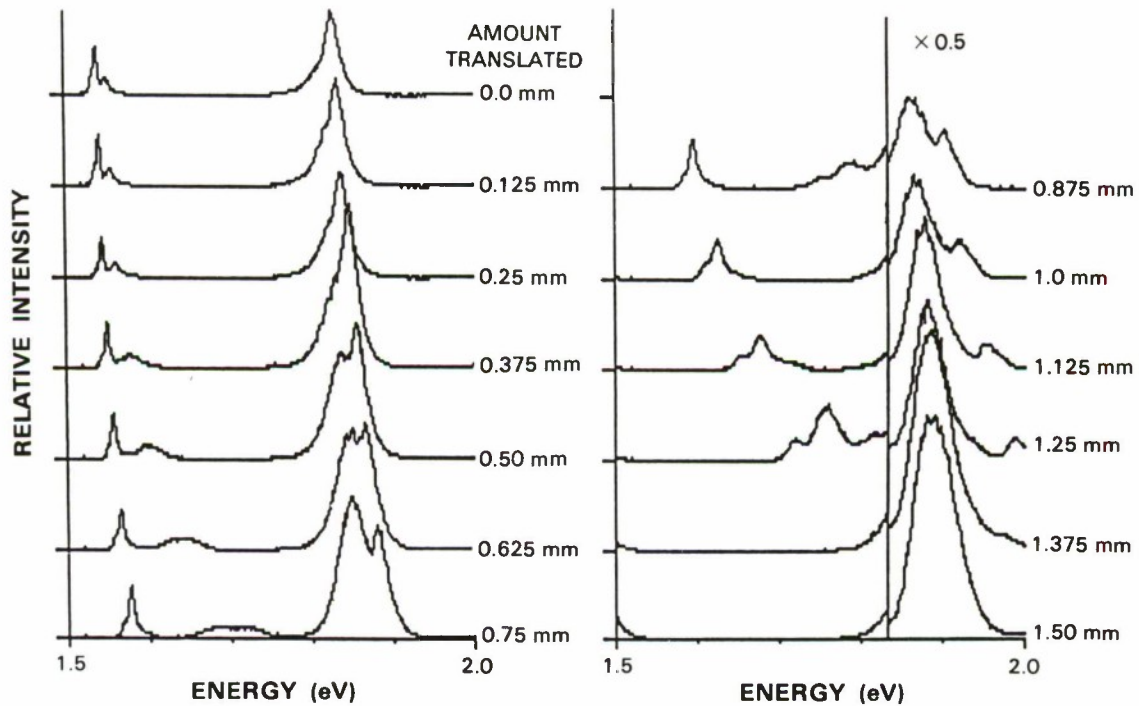
Figure 2-11. Photoluminescence data at 77 K from a typical growth run. The curves were taken at positions 125 μm apart. The excitonic features of the wells are easily seen in the colder region (top left) and the transition region. For this sample, they merge with the luminescence from the AlGaAs buffer layer in the hotter region (bottom right).

28

Several groups have achieved tapered[8-11] quantum wells by overgrowing etched grooves in substrates,[1-4] relying on the different growth rates of the different crystallographic planes. This technique achieves significant tapering at the expense of planarity, and is not capable of producing thickness variations on the horizontal wafer surfaces. By utilizing the temperature dependence of the Ga sticking coefficient[12,13] in a molecular-beam-epitaxy (MBE) system, QWs with estimated thickness variations of greater than 250 percent have been grown at points on a wafer 1 mm apart. This estimate was determined from photoluminescence data using a square well model, without including the influence of Al diffusion into the wells. With this growth technique, the surface remains relatively flat after the growth of the wells so that standard wafer processing can be employed.

The GaAs/AlGaAs QW structures studied consist of an AlGaAs buffer layer, 5 to 40 GaAs QWs separated by AlGaAs barrier layers, a 1-μm-thick AlGaAs cladding layer, and a 30-nm GaAs cap layer, all grown by MBE on a GaAs substrate. To locally control the substrate temperature, the substrates were mounted with indium on a slotted MBE mounting block (Figure 2-10). The surface temperature of the portions of the substrate over the gaps in the mounting block were found with a two-color infrared pyrometer to be 30° to 50°C colder than the portions over the indium-bonded regions when the block temperature was set at 710° to 720°C. The substrates were overgrown in the MBE system at block temperature of 715°C using an ion gauge arsenic flux of 1.5×10^5 Torr, an arsenic-to-gallium flux ratio of 24 to 1, and a gallium-to-aluminum flux ratio of 5 to 1. The shutters were timed to give a nominal 12-nm GaAs well width.

Photoluminescence data at 77 K from a typical growth run are shown in Figure 2-11. The excitonic features are easily seen in the colder region, the transition region, and, in most cases, the hotter region. The intensity and linewidth of the heavy-hole peaks indicate that the range of substrate temperatures used accommodated the material growth reasonably well, although we feel that more can be done to optimize the growth conditions. Figures 2-12 and 2-13 plot the peak energy of the heavy-hole exciton as a function of position on the wafer surface for two different growth runs. The data in Figure 2-12, taken for the same sample as the data in Figure 2-11, indicate uncoupled QWs with a well width of about 13 nm in the colder regions, getting narrower in the transition region until they form a superlattice. Finally, as shown in Figure 2-11 but not in Figure 2-12, the excitonic features of this sample merge with the luminescence from the AlGaAs buffer layer in the hotter region. The individual well dimensions in the hot region are estimated from the model to be less than 5 nm. Figure 2-13 corresponds to a sample with a much less dramatic change from region to region. In both of these samples, the transition region is about 1 mm wide. The trade-offs between transition-region length and well-thickness differences have not yet been examined.

W.D. Goodhue
J.J. Zayhowski
K.B. Nichols

29
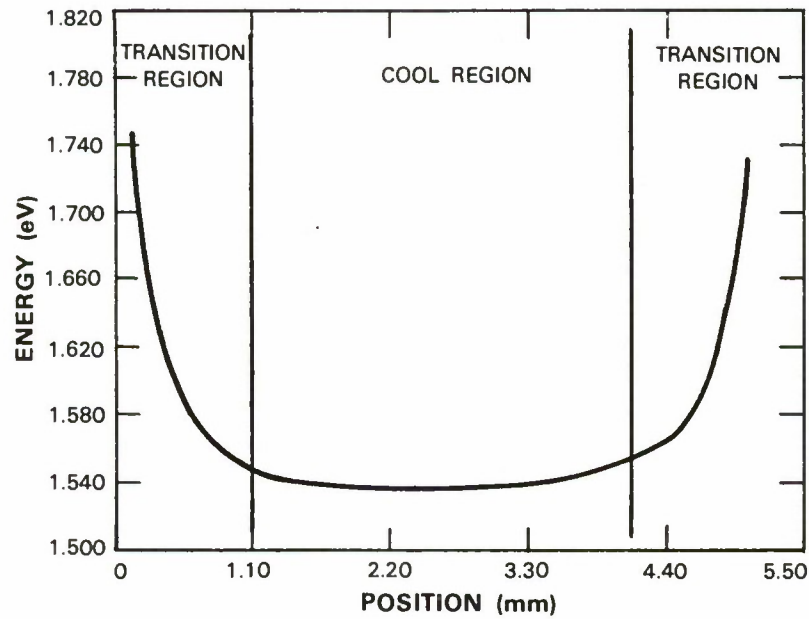
Figure 2-12. *The peak energy of the heavy-hole exciton as a function of position on the wafer surface, taken for the same sample as Figure 2-11.*
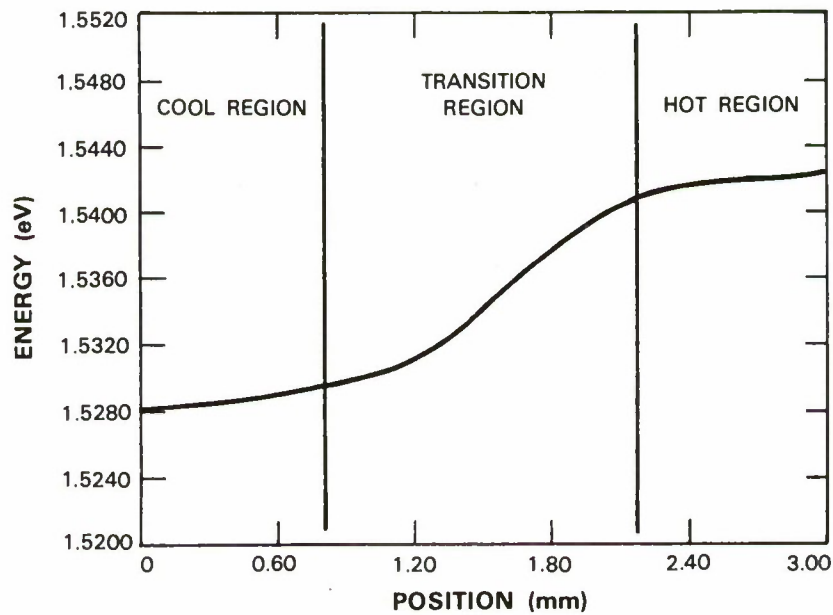
Figure 2-13. *The peak energy of the heavy-hole exciton as a function of position on the wafer surface for a sample with relatively small changes in QW width across the temperature-transition region.*

30

REFERENCES

1. P.A. Schulz, A. Sanchez, R.E. Fahey, and A.J. Strauss, in *Conference on Lasers and Electro-Optics Technical Digest Series 1987, Vol. 14* (Optical Society of America, Washington, DC, 1987), p. 296.

2. T.F. Johnson, Jr., R.H. Brady, and W. Proffitt, Appl. Opt. **21**, 2307 (1982).

3. Solid State Research Report, Lincoln Laboratory, MIT (1986:3), p. 19, DTIC AD-A178394.

4. *Ibid.* (1987:1), p. 28.

5. T.A. Driscoll, H.J. Hoffman, and R.E. Stone, J. Opt. Soc. Am. B **3**, 683 (1986).

6. S.E. Moody, J.M. Eggleston, and J.F. Seamans, IEEE J. Quantum Electron. **QE-23**, 335 (1987).

7. Solid State Research Report, Lincoln Laboratory, MIT (1987:1), p. 26.

8. J. Ralston, G.W. Wicks, and L.F. Eastman, J. Vac. Sci. Technol. B **4**, 594 (1986).

9. J.M. VanHove, P.R. Pukite, G.J. Whaley, A.M. Wowchak, and P.I. Cohen, J. Vac. Sci. Technol. B **3**, 1116 (1985).

10. W.T. Tsang and A.Y. Cho, Appl. Phys. Lett. **30**, 293 (1977).

11. S. Nagata, T. Tanaka, and M. Fukai, Appl. Phys. Lett. **30**, 503 (1977).

12. J.S. Smith, P.L. Derry, S. Margalit, and A. Yariv, Appl. Phys. Lett. **47**, 712 (1985).

13. E. Kapon, M.C. Tomargo, and D.M. Hwang, Appl. Phys. Lett. **50**, 347 (1987).

3. MATERIALS RESEARCH

3.1. PREPARATION OF SUPERCONDUCTING YBa$_2$Cu$_3$O$_x$ THIN FILMS BY OXYGEN ANNEALING OF MULTILAYER METAL FILMS

The preparation of bulk ceramic samples in the La-Ba-Cu-O (Reference 1) and Y-Ba-Cu-O (Reference 2) systems with superconducting transition temperatures T_c exceeding 30 and 90 K, respectively, has been followed by numerous efforts to prepare high-T_c thin films, which could have important applications in microelectronics. Such films have recently been obtained in the La-Sr-Cu-O and Y-Ba-Cu-O systems by sputtering[3-6] and electron-beam coevaporation[7,8] methods. In this report, we describe the preparation of superconducting YBa$_2$Cu$_3$O$_x$ thin films by a different method. As shown schematically in Figure 3-1, a multilayer metal film formed by sequential electron-beam evaporation of Cu, Ba, and Y is homogenized and oxidized by annealing in oxygen to form YBa$_2$Cu$_3$O$_x$. Since the thicknesses of the individual evaporated layers can be controlled very accurately, this method permits the metal concentrations in the superconducting films to be adjusted precisely and reproducibly. The method also has the advantage of utilizing standard commercial electron-beam evaporation equipment. Thus far, the best films we have prepared show the onset of superconductivity at 94 K and zero resistivity at 72 K.

A single-electron-gun, three-hearth vacuum system was used to deposit the metal layers on sapphire (Al$_2$O$_3$) and yttria-stabilized cubic zirconia (YSZ) single-crystal substrates, which were kept at ambient temperature during deposition. The deposition rate was 3 to 5 Å/s. Because Cu has a lower oxygen affinity than the other metals, in order to minimize interaction with the substrate a layer of Cu was deposited first, followed by layers of Ba and Y. This three-layer sequence was then repeated five times, for a total of 18 layers. The layer thickness was monitored with a quartz-crystal oscillator. (The oscillator was calibrated for Y and Cu by using a Dektak to
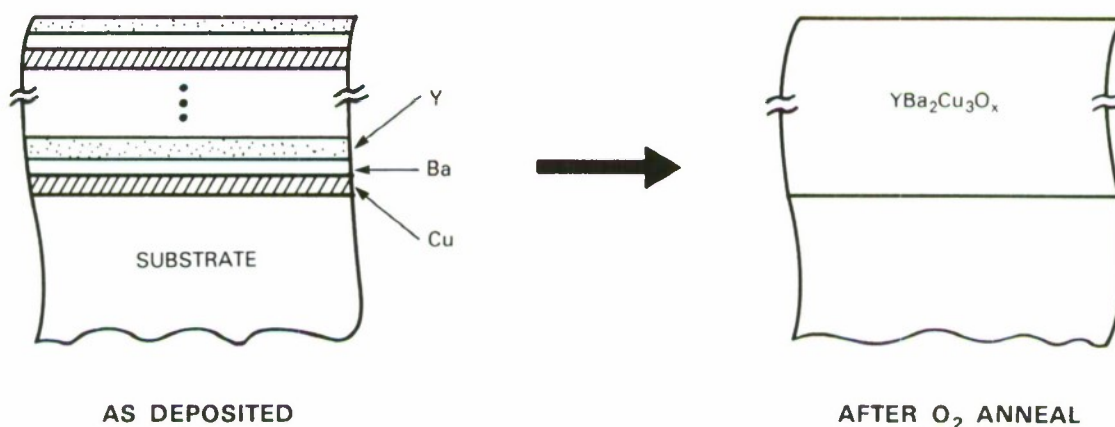
Figure 3-1.   Schematic diagram showing preparation of YBa$_2$Cu$_3$O$_x$ films by deposition of multilayer Cu-Ba-Y films followed by annealing in oxygen.

(a)
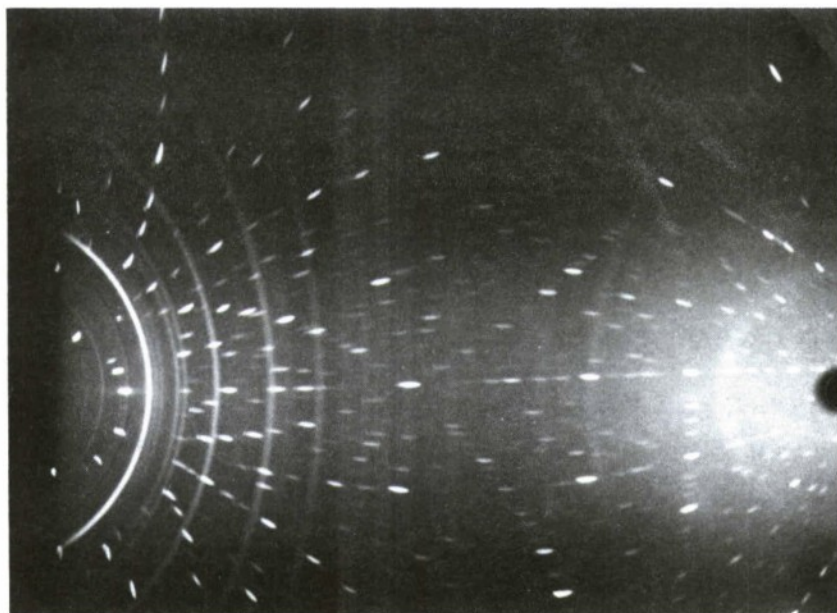
(b)
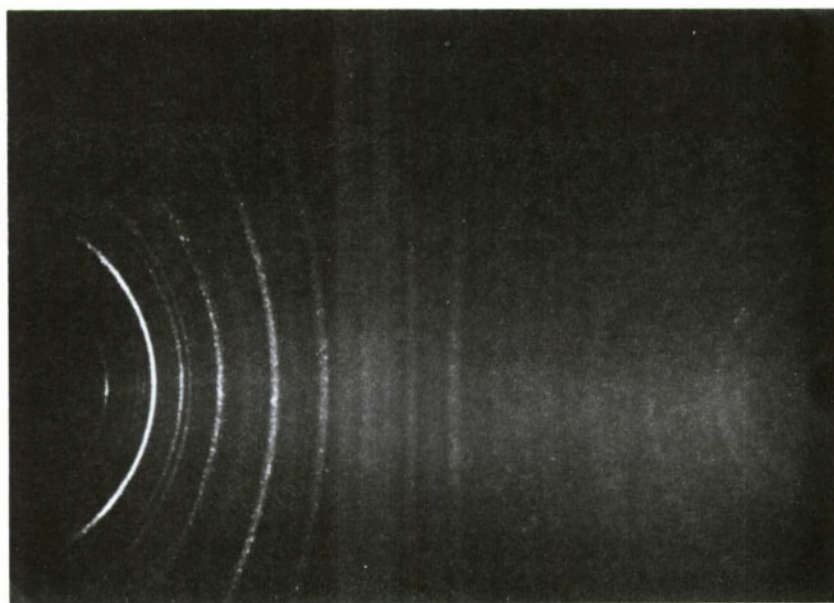
Figure 3-2. X-ray diffraction patterns taken with a Read camera for $YBa_2Cu_3O_x$ samples: (a) thin film on Al_2O_3 (spots are due to the substrate); (b) bulk ceramic.

34

measure the thickness of films of each metal. For Ba, the oscillator sensitivity was calculated from the bulk properties of the metal, because Ba films are too unstable in air to permit Dektak measurements.) The nominal thicknesses of the layers were either 10, 38, and 11 nm or 20, 76, and 22 nm for Y, Ba, and Cu, respectively, to obtain atomic ratios of 1:2:3. Thus, the total film thickness was either about 350 or 710 nm. The as-deposited films are mirror-smooth and have a silvery metallic appearance. X-ray diffraction measurements show that they consist of polycrystalline phases of Y, Ba, and Cu.

To form the superconducting phase, the metal films were annealed in flowing O_2 gas at 800° to 850°C for 0.5 to 4 h and then cooled to room temperature at a rate of ~2°C/min. The annealed films are black and noticeably roughened. Dektak measurements indicate a surface roughness of 20 to 30 nm for the films 350 nm thick and 100 to 150 nm for the films 710 nm thick.

Glancing-angle x-ray diffraction patterns obtained with a Read camera for a 710-nm-thick annealed film on Al_2O_3 and for a bulk ceramic single-phase specimen of $YBa_2Cu_3O_x$ are shown in Figures 3-2(a) and (b), respectively. The thin-film pattern contains all the major lines of the bulk pattern, but it also contains a few weak unidentified lines indicating the presence of a small percentage of another phase or phases. The film pattern gives no evidence of preferred orientation or texture.

The temperature dependence of resistivity for representative 710-nm-thick films processed side by side on Al_2O_3 and YSZ substrates is shown in Figures 3-3(a) and (b), respectively. For the film on Al_2O_3, the resistivity is about 5×10^3 $\mu\Omega$-cm at 300 K and initially increases with decreasing temperature. There is a broad superconducting transition with onset at 95 K and zero resistivity at 40 K. For the film on YSZ, the resistivity is only about 0.9×10^3 $\mu\Omega$-cm at 300 K and initially decreases linearly with decreasing temperature, reaching about 0.7×10^3 $\mu\Omega$-cm at 100 K. This temperature dependence is qualitatively similar to that observed for bulk superconducting samples of $YBa_2Cu_3O_x$, although the slope in the normal regime is considerably greater for good bulk samples. The superconducting transition for the film on YSZ is considerably sharper than for the film on Al_2O_3, with onset at 93 K and zero resistivity at 66 K. Our best film prepared on YSZ has an onset at 94 K and reaches zero resistivity at 72 K. At 4.2 K, the critical current density of this film is approximately 1×10^4 A/cm^2.

To assess the stability of the $YBa_2Cu_3O_x$ films, a series of resistivity-vs-temperature measurements was made on the film of Figure 3-3(b) over a period of 10 days. Between measurements the sample was stored under nitrogen gas, and after each measurement it was warmed up under nitrogen to prevent condensation of water vapor. The results are shown in Figure 3-4. The resistivity in the normal state gradually increased over the entire period, but the slope of the normal-state resistivity-vs-temperature curve did not change significantly. Both the superconductivity-onset temperature and the shape of the transition curve remained about the same, while the temperature for zero resistivity became progressively lower, reaching 60 K after 10 days.
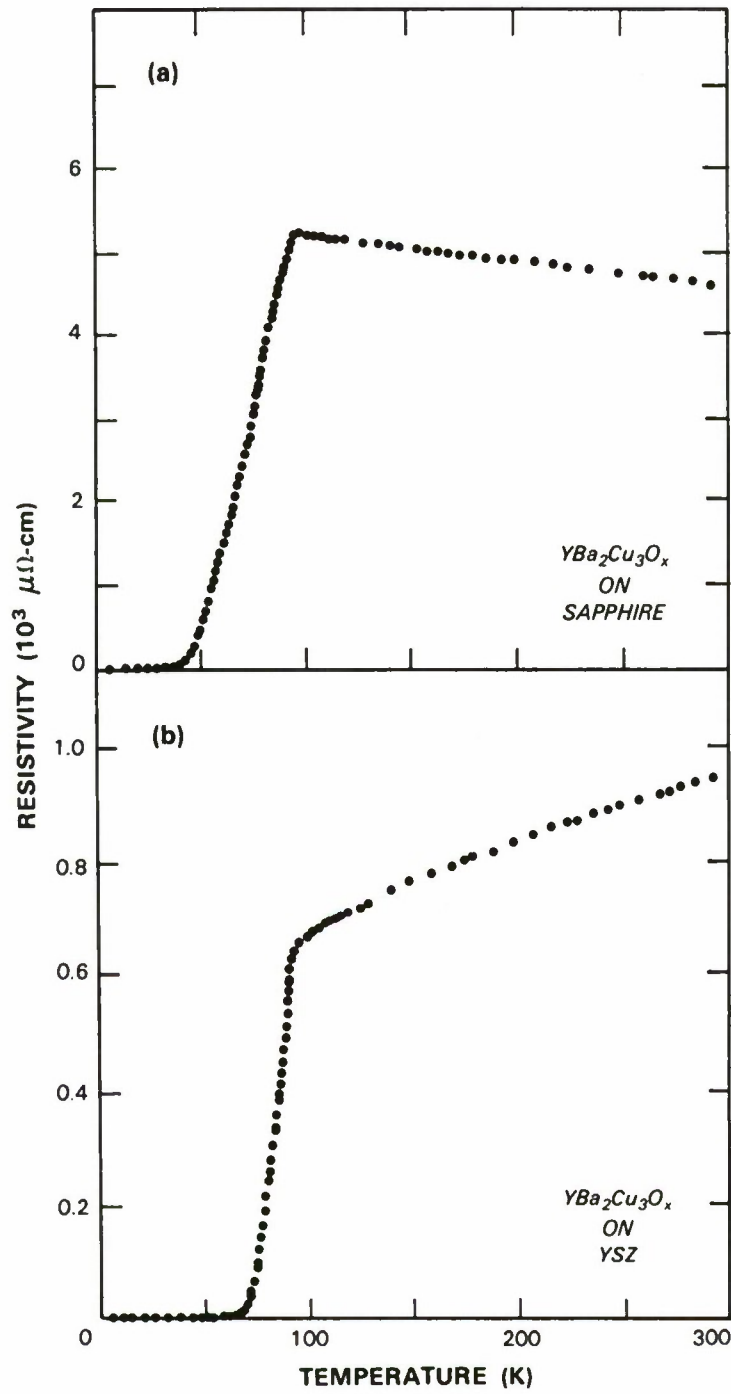
Figure 3-3. Temperature dependence of resistivity for $YBa_2Cu_3O_x$ thin films on (a) Al_2O_3 and (b) YSZ substrates.

36
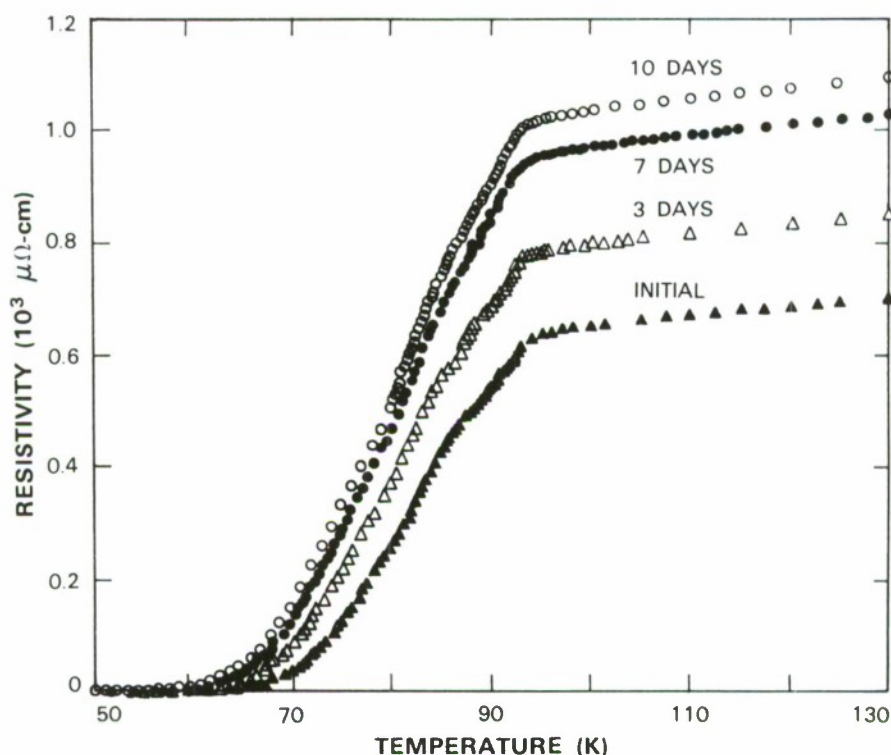
Figure 3-4.   Initial resistivity-vs-temperature curve for film of Figure 3-3(b) compared with curves measured after film was stored in nitrogen gas for 3, 7, and 10 days.

The present experimental results show that the substrate can have an appreciable effect on the superconducting properties of the film, as well as on the electrical properties in the normal state. In particular, both sets of properties are significantly worse for films on Al_2O_3 than for films on YSZ. This difference apparently results from chemical interaction with the Al_2O_3, since elemental depth profiles obtained by Auger analysis of our films on Al_2O_3 and YSZ show that the film-substrate interface is much more diffuse for the former than for the latter. Other workers have also reported[6,7] that $YBa_2Cu_3O_x$ films interact more strongly with Al_2O_3 than with YSZ. The Auger data also indicate that the overall Ba concentration in our films is less than the stoichiometric concentration in $YBa_2Cu_3O_x$. It is likely that this deficiency, which resulted because the calculation for the quartz-crystal oscillator overestimated the thickness of the deposited Ba layers, is partially responsible for the multiphase character of the films and therefore contributes to the broadening of the superconducting transitions.

<div style="text-align: right">

B-Y. Tsaur
M.S. DiIorio
A.J. Strauss

</div>

3.2. LOW-THRESHOLD GaAs/AlGaAs RIDGE-WAVEGUIDE LASERS ON Si

Since Windhorn *et al.*[9] first demonstrated GaAs/AlGaAs lasers on Si in 1984, considerable reduction in threshold current has resulted from improvement in the quality of heteroepitaxial GaAs/AlGaAs layers on Si and the employment of quantum-well laser structures. The lowest threshold current so far reported in the literature,[10] however, is more than 100 mA. We have now fabricated GaAs/AlGaAs double-heterostructure ridge-waveguide lasers on Si with pulsed threshold currents as low as 50 mA.

The laser structure was grown by organometallic vapor phase epitaxy (OMVPE) on an n^+ Si substrate oriented 2° off (100) toward (110). An n^+ GaAs buffer layer about 2 μm thick was deposited at Kopin Corporation (Taunton, MA) by the following procedure. The substrate was cleaned *in situ* at high temperature, a GaAs film 10 nm thick was deposited at 450° to 470°C, and the temperature was raised to 670°C to deposit the remainder of the layer. The following layers were then grown by OMVPE at Lincoln Laboratory: 0.2-μm n^+ GaAs, 1.0-μm n $Al_{0.6}Ga_{0.4}As$, 0.03-μm nominally undoped GaAs active, 0.7-μm p $Al_{0.6}Ga_{0.4}As$, and 0.1-μm p^+ GaAs cap. The growth temperature was 780°C.

The double-crystal x-ray rocking curve for an OMVPE GaAs/AlGaAs layer (Figure 3-5) shows overlapping GaAs and AlGaAs lines with peaks separated by about 200 arc sec. Although
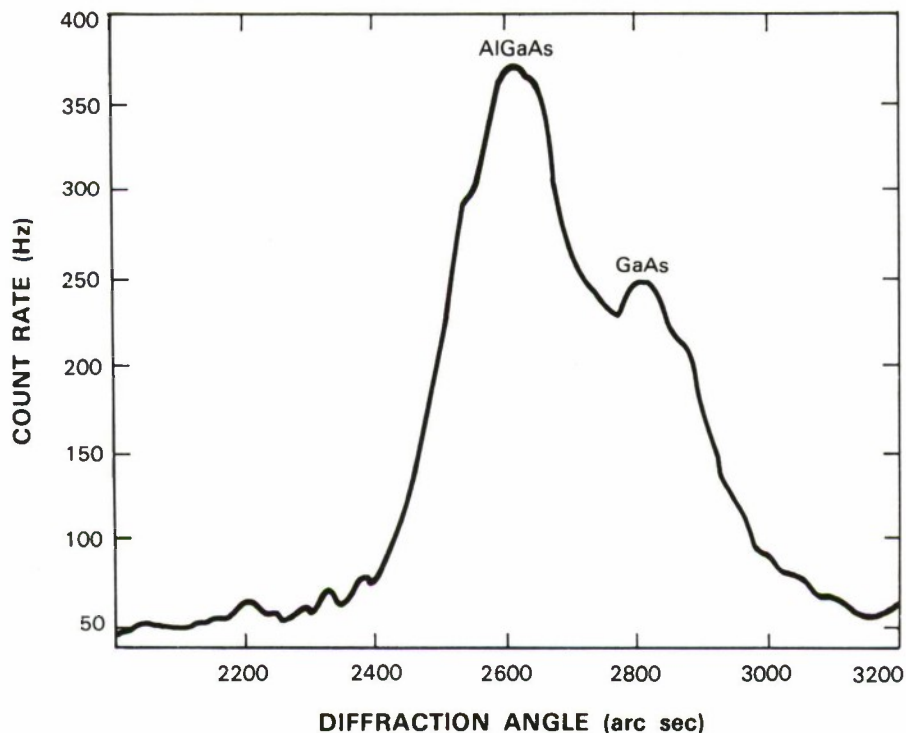
Figure 3-5. X-ray rocking curve for GaAs/AlGaAs layer grown on Si by OMVPE.

38

the half-widths of the two lines cannot be measured accurately because of the overlap, they are estimated to be less than 200 arc sec. Half-widths as low as 130 arc sec have been measured for 3-μm-thick GaAs layers on Si grown by OMVPE at Kopin Corporation.

Figure 3-6 is a scanning electron micrograph of a cross section through one of the ridge-waveguide lasers. The width of the ridge is 4 μm. The ridge was formed by reactive ion etching of the GaAs/AlGaAs layer using a BCl$_3$/Ar mixture, which has equal etch rates for GaAs and AlGaAs and therefore permits easy control of the etch depth. Lateral current confinement was accomplished by using SiO$_2$ to prevent electrical contact outside the ridge. The laser facets were formed by cleaving through the GaAs/AlGaAs layer and the Si substrate after the Si had been thinned to about 70 μm.

Figure 3-7 shows the light output vs current characteristic obtained with 200-ns current pulses for a ridge-waveguide laser with a cavity length of 380 μm. The threshold current is 50 mA, and the differential quantum efficiency is about 10 percent per facet. No abnormal delay was observed in the pulse response of this device. The emission spectrum at 60 mA shows a predominant single longitudinal mode. The mode separation of about 10 Å corresponds to the position of a crack located 110 μm from one facet.

Figure 3-8 shows the light output vs current characteristic obtained with 200-ns current pulses for a 200-μm-wide by 380-μm-long GaAs/AlGaAs broad-area laser on Si. The threshold current is 220 mA, corresponding to an average threshold current density of about 300 A/cm^2. The pulse response at 2 mW output shows a long delay in laser emission, indicating the presence of saturable absorbers, while a fast rise time is observed at 8 mW. The near-field pattern of the broad-area lasers shows severe nonuniformities. Lasing occurs predominantly in a single filament. Since the mirror facets appear uniform, the filamentation is probably due to nonuniformity in the GaAs/AlGaAs material.

H.K. Choi
M.K. Connors
B-Y. Tsaur

3.3. AVALANCHE-INDUCED DRAIN-SOURCE BREAKDOWN IN SILICON-ON-INSULATOR n-MOSFETS

As the dimensions of n-channel MOSFETs are reduced, avalanche-induced drain-source breakdown becomes a limiting factor in their operation. The breakdown of n-MOSFETs fabricated on bulk silicon substrates involves two positive-feedback processes: electron impact ionization near the drain junction, and electron emission from the bulk-source junction. The same basic mechanisms apply to n-MOSFETs fabricated in silicon-on-insulator (SOI) films, but the breakdown characteristics of the SOI devices are different because the substrate is floating and the silicon thickness is limited. In this report, we outline a drain-source breakdown model that takes these effects into account, and we compare the predictions of this model with the breakdown characteristics observed for SOI n-MOSFETs.

Cr/Au
SiN$_x$
p$^+$ GaAs
p Ga$_{0.4}$Al$_{0.6}$As
UNDOPED GaAs
n Ga$_{0.4}$Al$_{0.6}$As

n$^+$ GaAs

n$^+$ Si

20KV X10000   1U 022 8744   '87
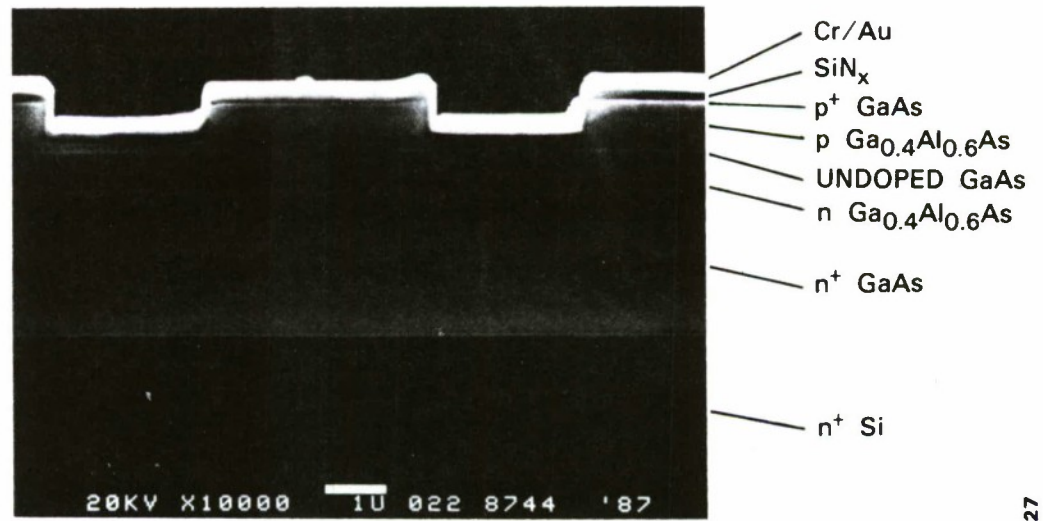
87265-27

Figure 3-6. Cross-sectional scanning electron micrograph of GaAs/AlGaAs ridge-waveguide laser on Si.
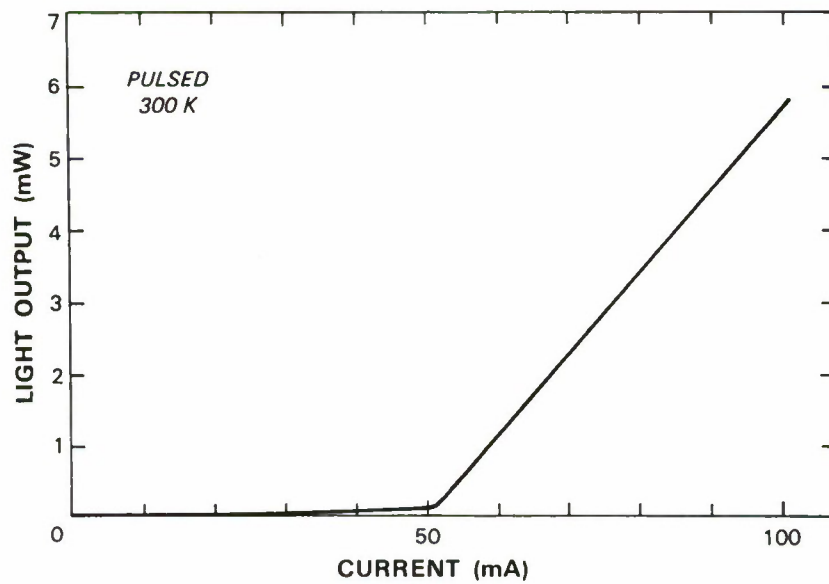
87265-28

Figure 3-7. Light output vs current characteristic of a GaAs/AlGaAs ridge-waveguide laser on Si.

40
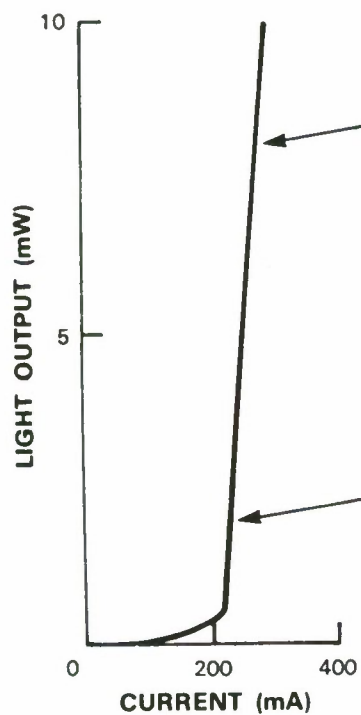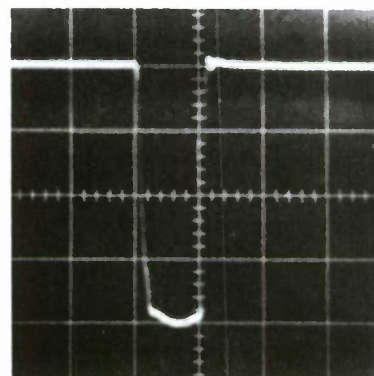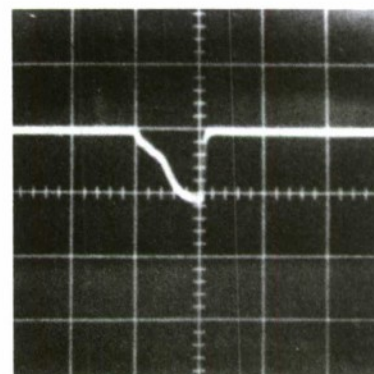
Figure 3-8. Light output vs current characteristic and pulse response of a GaAs/AlGaAs broad-area laser on Si.
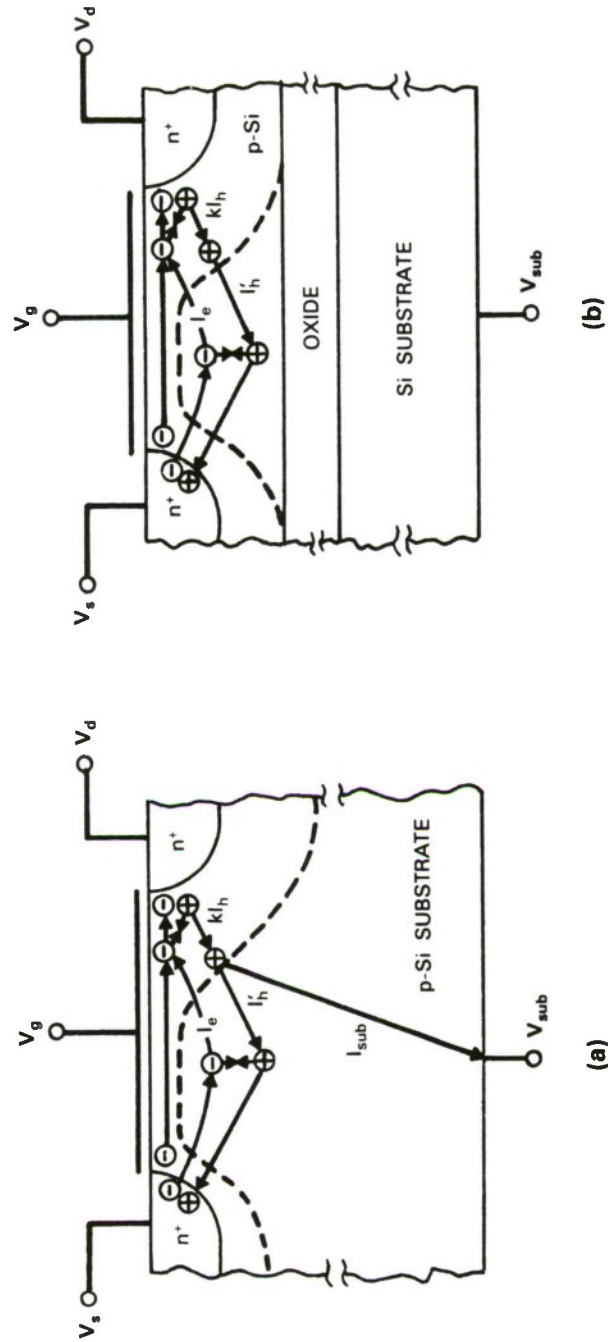
Figure 3-9. Schematic diagrams showing current flow in (a) bulk-silicon and (b) SOI n-channel MOSFETs operated in the saturation regime. Dashed lines represent boundaries of depleted regions.

87265-11

42

The current flow in bulk-silicon and SOI n-channel MOSFETs operated in the saturation regime is shown schematically in Figures 3-9(a) and (b), respectively. Near the drain-channel junction, the hole current I_h is generated by field-enhanced electron impact ionization. I_h is related to the multiplication factor M and the channel current I_{ch} by the expression

$$I_h = (M - 1) I_{ch} \quad . \tag{3-1}$$

Because of losses due to the hole flow into the channel region, only a fraction kI_h of the generated hole current flows through the bulk region of n-channel MOSFETs. For a bulk-silicon device, as illustrated in Figure 3-9(a), this fraction is equal to the sum of the substrate current I_{sub} and the hole current I_h' flowing through the bulk region toward the source junction:

$$kI_h = I_{sub} + I_h' \quad . \tag{3-2}$$

The ohmic drop induced by I_{sub} raises the bulk-to-source potential V_{bs} and forward biases the bulk-source junction, increasing I_h'.

Figure 3-10 plots the calculated kI_h-V_{bs} relationship for a bulk-silicon n-MOSFET with $k = 0.8$, $R_{sub} = 10$ kΩ, and $\alpha_T\gamma = 0.85$, where R_{sub} is the substrate spreading resistance, α_T is the base transport factor for a lateral npn transistor, and γ is the injection efficiency of the source junction. At low I_h, most of the generated holes flow into the substrate contact and I_h' is negligible. When I_h increases sufficiently for V_{bs} to reach the turn-on value $V_{bs,on}$, I_h' becomes dominant over I_{sub} and most of the hole current will flow into the source region.
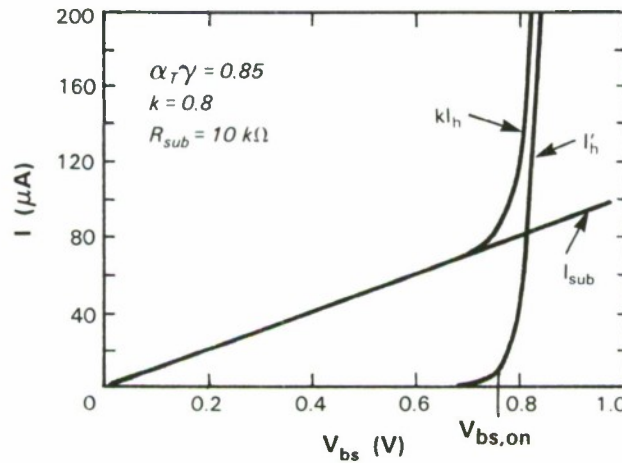
Figure 3-10. *Calculated values of kI_h, I_h', and I_{sub} vs V_{bs} for bulk-silicon n-MOSFET. For SOI devices, $I_{sub} = 0$ and $kI_h = I_h'$.*

For an SOI device, because the silicon film is insulated from the substrate, most of the generated holes are forced to flow into the source region, as illustrated in Figure 3-9(b). In this case,

43

$$kI_h \approx I_h'$$ (3-3)

where the I_h'-V_{bs} relationship is the same as shown in Figure 3-10 for a bulk-silicon device. For typical device parameters, therefore, the bulk-source junction of the SOI n-MOSFET is turned on (i.e., $V_{bs} = V_{bs,on}$) at a much lower value of kI_h than its bulk-silicon counterpart.

When the bulk-source junction is turned on, electrons will be injected from the source into the bulk region. A fraction k' of the injected electrons is collected near the high-field drain region, further increasing the hole current generation. If I_e is the electron current flowing into the high-field region, the total drain current I_{ds} is given by

$$I_{ds} = M(I_{ch} + I_e) + \frac{(1-k')}{k'} I_e \quad .$$ (3-4)

For SOI n-MOSFETs,

$$
\begin{aligned}
I_h &= (M-1)(I_{ch} + I_e) \\
&= \frac{(M-1) I_{ch}}{1 - (M-1) k' \dfrac{\alpha_T \gamma}{1 - \alpha_T \gamma} k} \quad .
\end{aligned}
$$ (3-5)

Avalanche breakdown occurs when the denominator of Equation (3-5) approaches zero. Therefore, the multiplication factor at breakdown, which we designate as M_{aval}, is given by

$$M_{aval} - 1 = \frac{1 - \alpha_T \gamma}{k' \alpha_T \gamma k} = \frac{1}{k' \beta k}$$ (3-6)

where β is the effective current gain of a lateral npn transistor. For bulk-silicon n-MOSFETs, the expression for $(M_{aval} - 1)$ is approximately the same as Equation (3-6).

According to the above analysis, drain-source breakdown occurs only when both the source turn-on and avalanche multiplication conditions are satisfied. For bulk-silicon devices, the source turn-on condition is the limiting breakdown mechanism at small gate bias, while the avalanche multiplication condition dominates at large gate bias. For SOI n-MOSFETs, the source junction generally turns on before the multiplication factor becomes large enough for avalanche breakdown. Therefore, avalanche multiplication is the limiting breakdown mechanism for SOI n-MOSFETs under all gate-bias conditions, and the breakdown voltage BV_{ds} is the value of the drain-source voltage V_{ds} at which $(M-1)$ becomes equal to $(M_{aval} - 1)$.

To test the breakdown model, the saturation drain-source I-V characteristics for representative SOI n-MOSFETs have been calculated from the equation obtained by replacing the quantities M, I_{ch}, and I_e on the right side of Equation (3-4) with the appropriate expressions in terms of V_{ds}. We find that good agreement with our experimental results can be obtained by adopting reasonable values for the parameters k, k', and β. This agreement is illustrated in Figures 3-11(a)

and (b) where the calculated I_{ds}-V_{ds} curves (dashed lines) for n-MOSFETs with gate lengths of 2 and 5 μm are compared with experimental curves (solid lines) measured at $V_g = 2$ and 4 V for such devices fabricated on SOI wafers prepared by zone-melting recrystallization (ZMR).

In a series of experiments to determine the qualitative dependence of BV_{ds} on key structural and operating parameters of SOI n-MOSFETs, we found that BV_{ds} increases with increasing channel length L_{eff} and increasing positive substrate bias voltage but decreases with increasing silicon film thickness. These observations can be explained by using the breakdown model to predict the qualitative dependence of k, β, and k' on the device parameters. For example, an increase in L_{eff} reduces both k and k' because it permits larger fractions of the holes generated by impact ionization at the drain-channel junction and the electrons injected from the source into the bulk region to be removed by recombination. From the base-width dependence of current gain in a lateral bipolar transistor, it follows that an increase in L_{eff} also reduces β. Consequently, increasing L_{eff} increases $(M_{aval} - 1) = 1/k\beta k'$ and therefore BV_{ds}.

The breakdown characteristics of SOI and bulk-silicon n-MOSFETs are compared in Figure 3-12, where the measured values of BV_{ds} are plotted against V_{gs} for two representative devices. For V_{gs} up to 5 V, BV_{ds} is higher for the bulk device than for the SOI device, but above this value the SOI device has the higher breakdown voltage. This behavior is readily explained by the proposed breakdown model.

For the higher values of V_{gs}, avalanche multiplication is the limiting breakdown mechanism for both bulk-silicon and SOI n-MOSFETs. For devices with the same geometry, the values of k, β, and k' are lower for the SOI device because the recombination lifetime is shorter than in bulk silicon. Therefore $(M_{aval} - 1)$ and BV_{ds} are higher for the SOI device. As V_{gs} is decreased, however, source turn-on eventually becomes the limiting breakdown mechanism for bulk-Si devices. At sufficiently low values of V_{gs}, the value of V_{ds} required for source turn-on in a bulk-silicon device becomes even higher than the value sufficient to produce avalanche multiplication in a similar SOI device. Thus, in this regime BV_{ds} is higher for the bulk device than for the SOI device.

K.K. Young
J.A. Burns
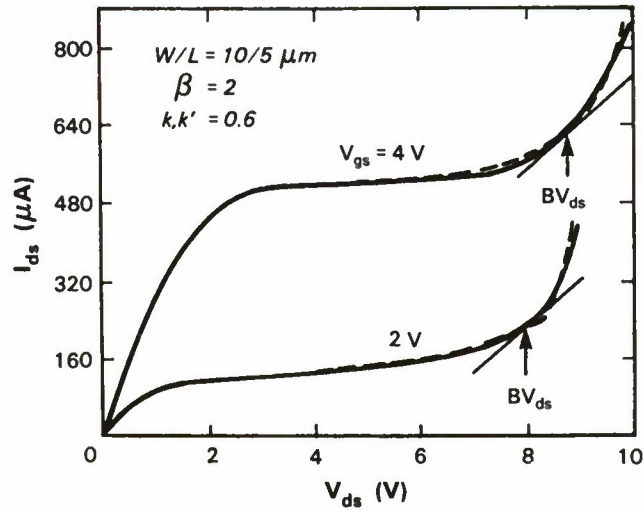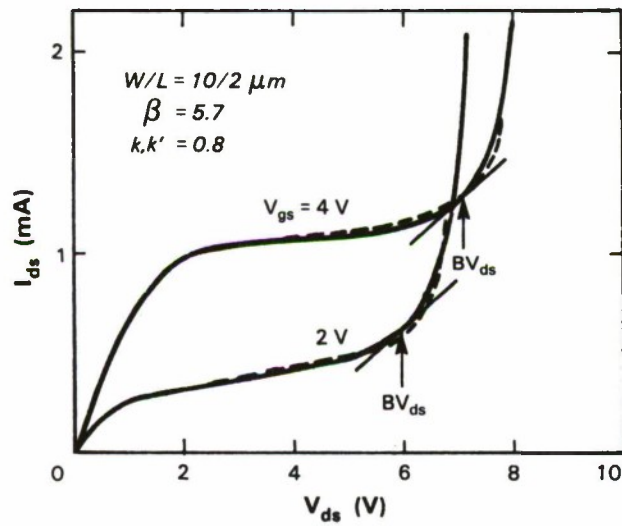
Figure 3-11. Comparison of calculated I_{ds}-V_{ds} characteristics (dashed curves) in the breakdown region with measured results (solid curves) for (a) 5-μm and (b) 2-μm SOI n-MOSFETs. The breakdown voltage is taken to be the value of V_{ds} when $dI_{ds}/dV_{ds} = 0.05$ (W_{eff}/L_{eff}) mS.
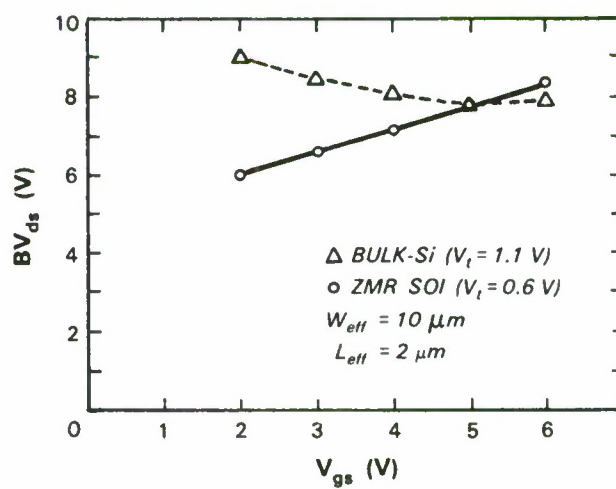
Figure 3-12. Measured values of BV_{ds} vs V_{gs} for SOI and bulk-Si n-MOSFETs.

47

REFERENCES

1. J.G. Bednorz and K.A. Müller, Z. Phys. **B64**, 189 (1986).

2. M.K. Wu, J.R. Ashburn, C.J. Torng, P.H. Hor, R.L. Meng, L. Gao, Z.J. Huang, Y.Q. Wang, and C.W. Chu, Phys. Rev. Lett. **58**, 908 (1987).

3. S. Nagata, M. Kawasaki, M. Funabashi, K. Fueki, and H. Koinuma, Jpn. J. Appl. Phys. **26**, L410 (1987).

4. N. Terada, H. Ihara, M. Hirabayashi, K. Senzaki, Y. Kimura, K. Murata, and M. Tokumoto, Jpn. J. Appl. Phys. **26**, L508 (1987).

5. H. Adachi, K. Setsune, T. Mitsuyu, K. Hirachi, Y. Ichikawa, T. Kamada, and K. Wasa, Jpn. J. Appl. Phys. **26**, L709 (1987).

6. M. Kawasaki, S. Nagata, Y. Sato, M. Funabashi, T. Hasegawa, K. Kishio, K. Kitazawa, K. Fueki, and H. Koinuma, Jpn. J. Appl. Phys. **26**, L738 (1987).

7. R.H. Hammond, M. Naito, B. Oh, M. Hahn, P. Rosenthal, A. Marshall, N. Missert, M.R. Beasley, A. Kapitulnik, and T.H. Geballe, in *Extended Abstracts, High Temperature Superconductors, 1987 MRS Spring Meeting*, D.B. Gubser and M. Schluter, Eds. (Materials Research Society, Pittsburgh, 1987), p. 169.

8. R.H. Koch, R.B. Laibowitz, P. Chaudhari, R.J. Gambino, G.J. Clark, A.D. Marwick, and C.J. Umbach, in *Extended Abstracts, High Temperature Superconductors, 1987 MRS Spring Meeting*, D.B. Gubser and M. Schluter, Eds. (Materials Research Society, Pittsburgh, 1987), p. 81.

9. T.H. Windhorn, G.M. Metze, B-Y. Tsaur, and J.C.C. Fan, Appl. Phys. Lett. **45**, 309 (1984), DTIC AD-A147320.

10. H. Shiraishi, R. Yamada, N. Matsui, and M. Umeno, Jpn. J. Appl. Phys. **26**, L1012 (1987).

4. MICROELECTRONICS

4.1. CCD VECTOR-MATRIX PRODUCT DEVICE

Charge-coupled devices (CCD) are well suited for real-time signal processing applications, particularly those requiring a large number of computations with processors of a limited size and power. A CCD vector-matrix product (VMP) device designed to perform a 16-point discrete cosine transform (DCT) has been fabricated and reported previously.[1] Recent test results indicate that the DCT device has 60-dB dynamic range and –40-dB harmonic distortion. Clocked at 5 MHz, the device performs 5 billion computations per second. A new CCD VMP device which is capable of performing a 16-point complex discrete Fourier transform (DFT) has been designed, and wafer fabrication has started. In this report, we describe the recent DCT test results and some of the design features of the DFT device and its expected performance.

A block diagram of the DCT device can be seen in Figure 4-1 of Reference 1. For a given input vector g_n, the device computes a vector-matrix product h_k, where

$$h_k = \sum_{n=1}^{16} g_n \cos (2\pi nk/16)$$

for $k = 1,2,...,16$. The dynamic range of the DCT device has been measured for the case when the 16 elements of the input vector are identical and equal to V_{in}, i.e., when a common input voltage V_{in} is applied to all the 16 input gates. The output vector then consists of all zero elements except at $k = 16$ (i.e., $V_{out} = h_{16}$). The range over which V_{out} is linear with respect to V_{in} was determined, and the result is plotted in Figure 4-1. It demonstrates that the device has more than 60-dB dynamic range. The accuracy of the device has also been measured. The difference of the measured h_k and the calculated h_k is computed and defined as h_{error} for all k's. For the limited set of input vectors that we used (there are potentially 2^{256} different input vectors), all the h_{error} values are less than ± 15 mV. Since the maximum V_{out} is 1.35 V, the worst error generated by the device is –39 dB. All the experiments were performed at a 5-MHz clock rate.

A block diagram of a CCD DFT device is shown in Figure 4-2. The input vector consists of a real component $g_{r,n}$ and an imaginary component $g_{i,n}$:

$$g_n = g_{r,n} + jg_{i,n}$$

where $n = 1,2,...,16$. The device is designed to compute a 16-point Fourier transform h_k of the input vector g_n:
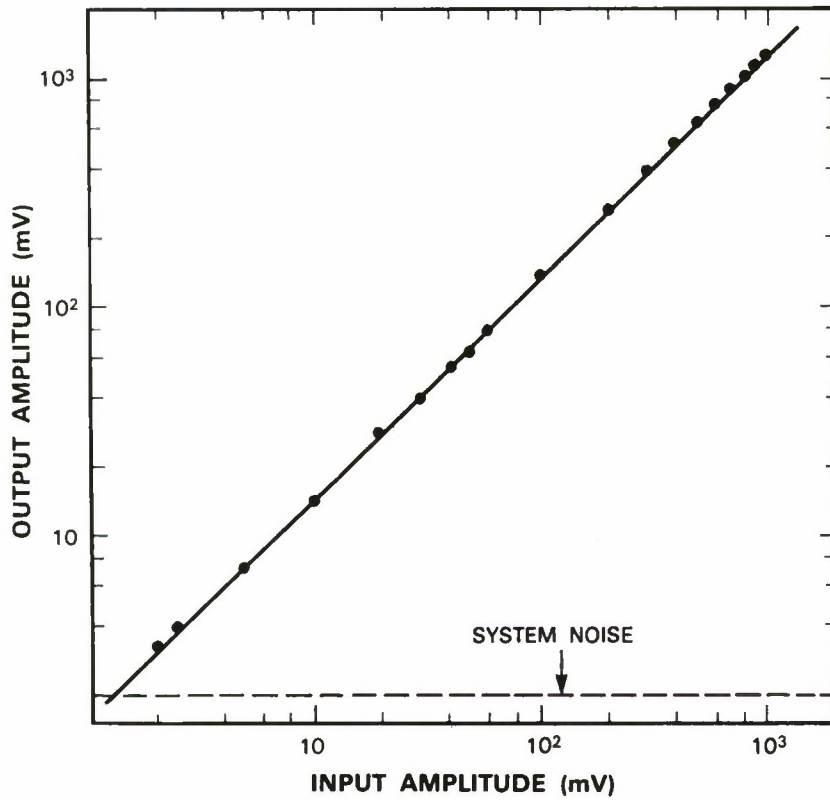
$$h_k = \sum_{n=1}^{16} g_n \exp [j2\pi nk/16] \qquad .$$

49

Figure 4-1. Dynamic range of the DCT device.

$$h_k = \sum g_n \exp [j2\pi nk/16]$$

Figure 4-2. CCD DFT device block diagram.

g: *INPUT TIME SAMPLES*

h: *OUTPUT SPECTRUM*
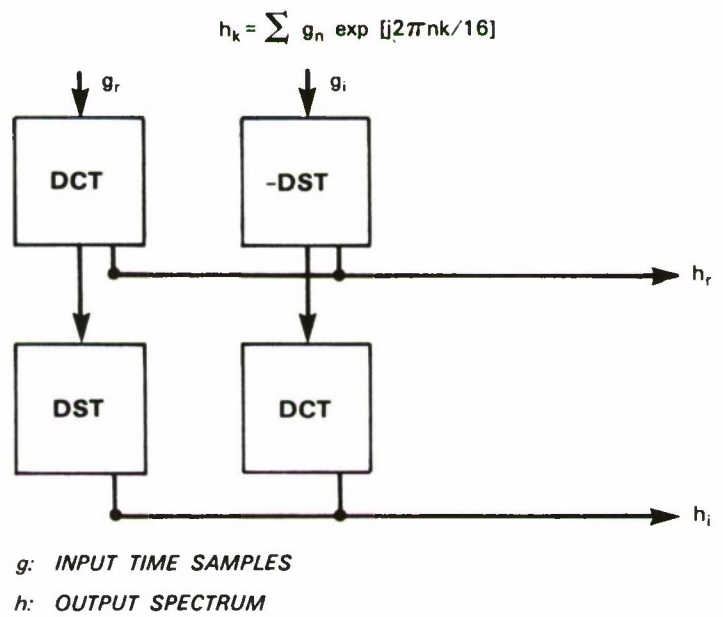
The real and imaginary components of the output vector can be written as

$$h_{r,k} = \sum_{n=1}^{16} [g_{r,n} \cos (2\pi nk/16) - g_{i,n} \sin (2\pi nk/16)]$$

$$h_{i,k} = \sum_{n=1}^{16} [g_{r,n} \sin (2\pi nk/16) + g_{i,n} \cos (2\pi nk/16)]$$

One can see that the DFT chip in Figure 4-2 is a direct implementation of the above vector-matrix product equation. The DFT device has been designed and its layout is shown in Figure 4-3. The chip size is 7×9 mm with a 5-μm design rule and is designed based on a double-polysilicon and double-metal process. Wafer fabrication has started during this reporting period. The chip is designed to perform 10 billion multiplications per second and dissipate less than 2 W.

A.M. Chiang   G.A. Lincoln

P.C. Bennett   J.H. Reinold

B.B. Kosicki   K.F. Johnson

R.W. Mountain

4.2. HARMONIC MULTIPLICATION USING RESONANT TUNNELING

A typical current-voltage (I-V) curve for a double-barrier resonant-tunneling diode is shown in Figure 4-4. The presence of a peak and valley in the I-V curve, combined with the overall antisymmetry about the origin [i.e., $I(V) = -I(-V)$], offers the potential for efficient odd-harmonic generation when biased near $V = 0$. The key lies in pumping the diode so that the peak amplitude of the voltage across the diode occurs above the resonant current peak. This causes at least three local maxima to occur in the diode current waveform over one cycle, corresponding to third or higher odd-harmonic generation.

To demonstrate this effect, we fit the I-V curve of Figure 4-4 with a seventh-order polynomial. The diode is assumed to be driven by a source having internal impedance less than the minimum negative resistance of the double-barrier diode, so that the current across the diode is a single-valued function of the drive voltage. Figure 4-5 shows the numerically determined voltage and current waveforms for a 50-Ω source impedance and 0.5-V amplitude. The local maxima in the current waveform, if equally spaced in phase, should lead to a strong fifth-harmonic component in the current power spectrum.

Figure 4-6 shows the experimental power spectrum for a resonant-tunneling diode when mounted in a 50-Ω coaxial circuit and pumped at 4.25 GHz. The calculated power spectrum for this device is shown in Figure 4-7. As expected, there is a complete absence of even harmonics and a predominance of the fifth among the odd harmonics. The measured fifth-harmonic efficiency is about 0.5 percent, which agrees well with that calculated. Although this efficiency is comparable with that of current state-of-the-art Schottky-diode quintuplers, it is significantly less

Real Input

Imaginary Input

Real Output

DCT

-DST

DST

DCT

Fixed Weight Multiplier

Imaginary Output

D F T
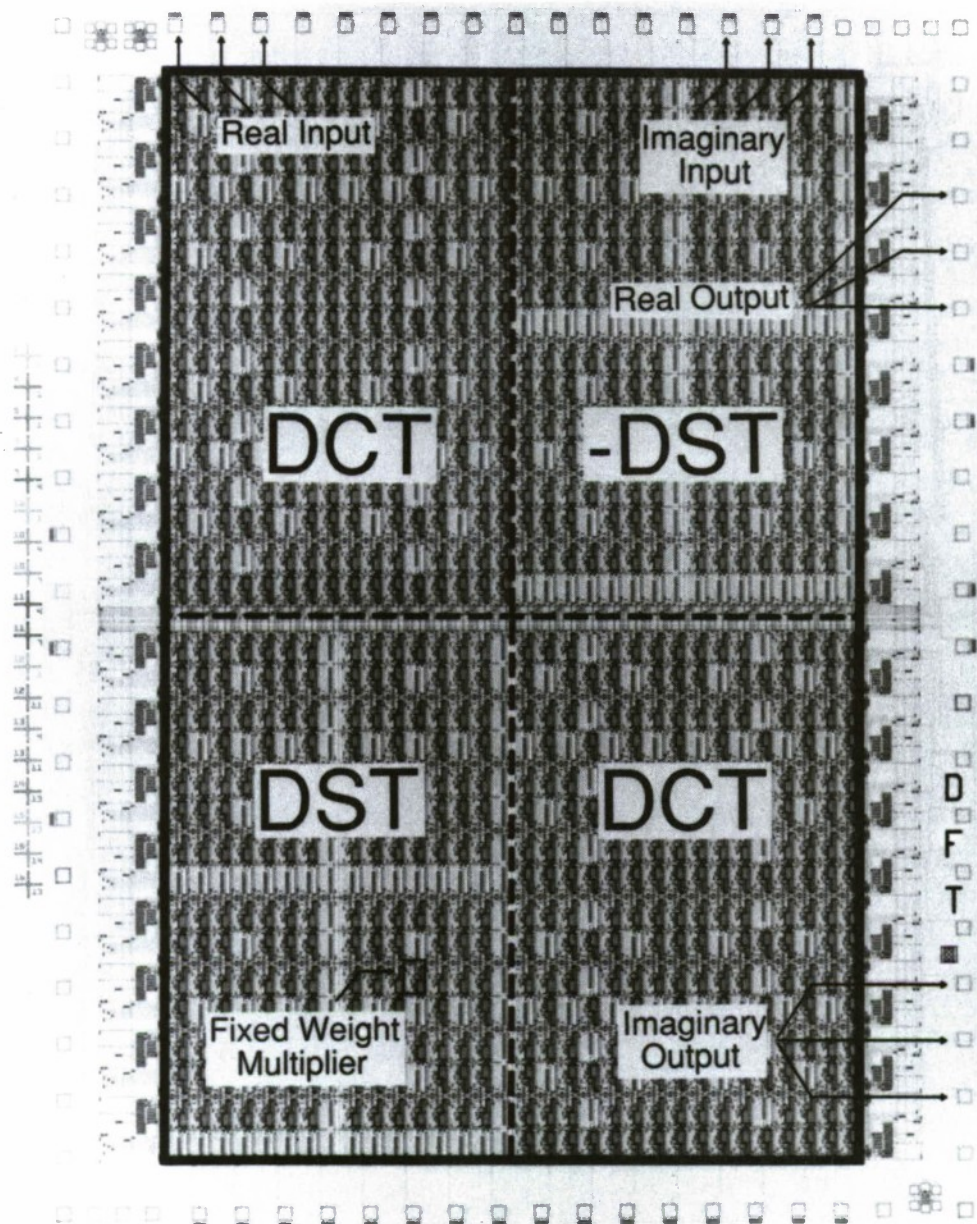
Figure 4-3. Layout of DFT device.

Figure 4-4. Typical current-voltage (I-V) curve of a double-barrier resonant-tunneling diode.
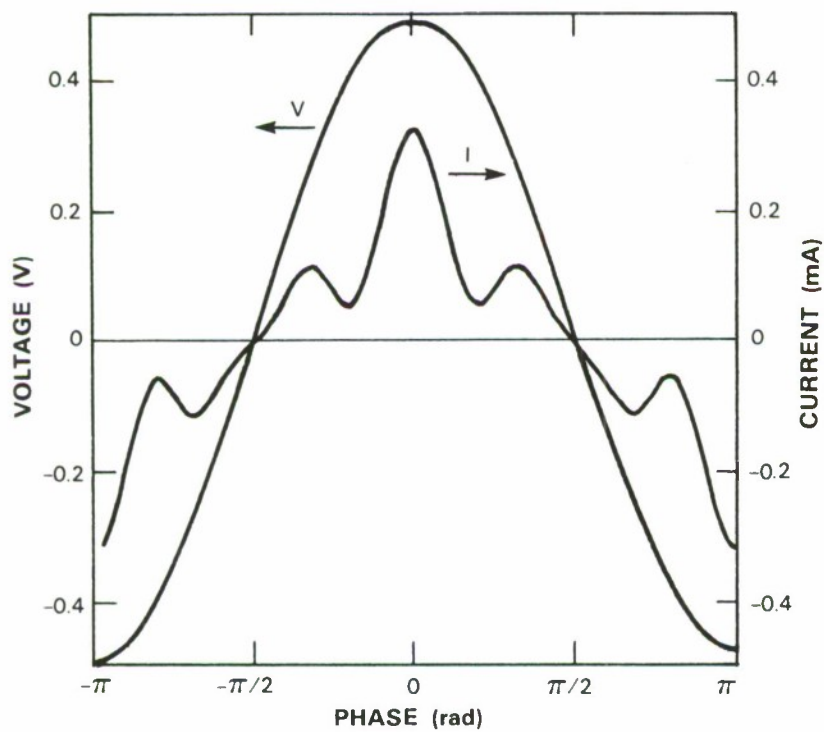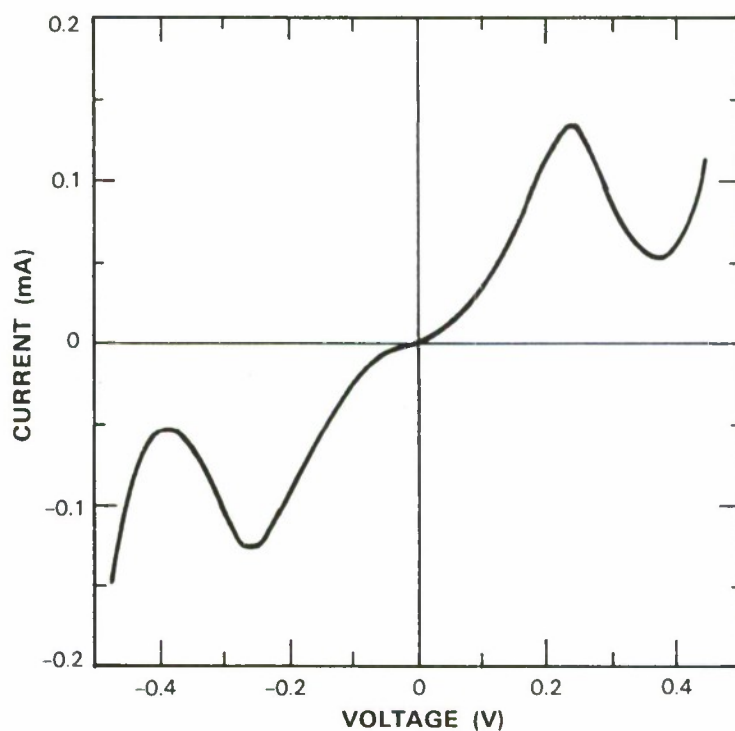
Figure 4-5. Calculated voltage and current waveforms for the I-V curve of Figure 4-4 when driven by a pump with a 50-Ω source impedance and 0.5-V amplitude.

53
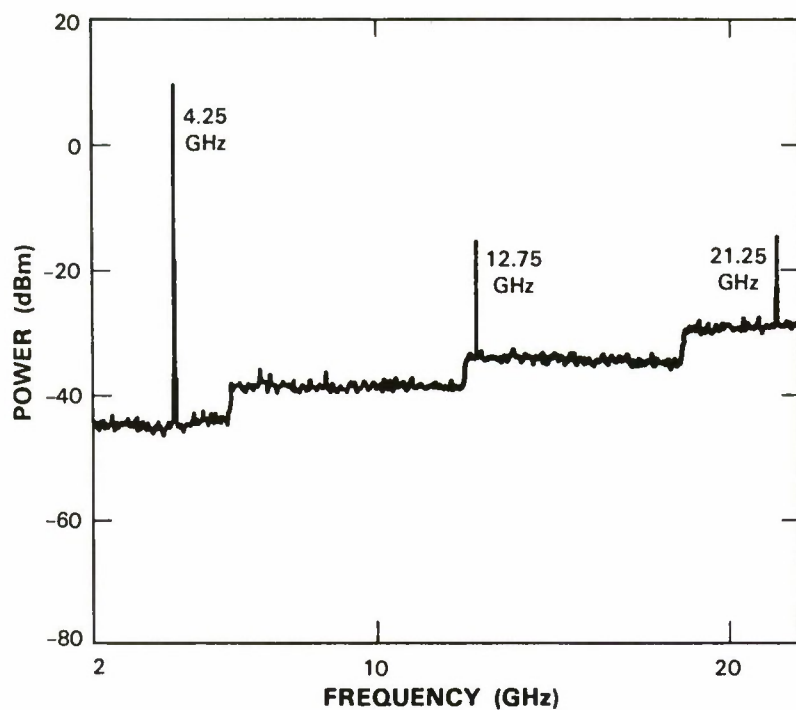
Figure 4-6. Output power of a resonant-tunneling multiplier in a coaxial mount when pumped at 4.25 GHz.
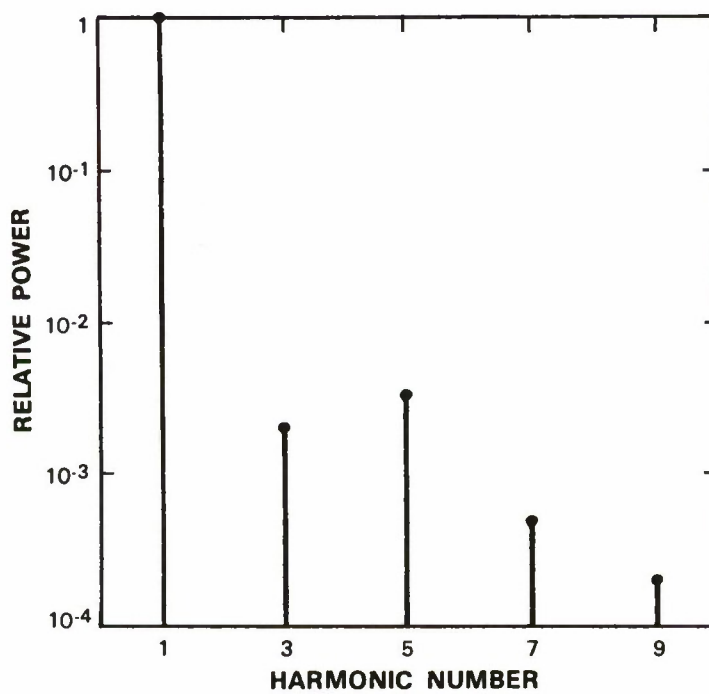
Figure 4-7. Power spectrum calculated for the device used to obtain Figure 4-6.

than could be obtained with an optimized I-V curve and load. We calculate that an efficiency of several percent could be achieved in that case.

The resonant-tunneling multiplier has several distinct advantages over existing resistive multipliers, which are usually based on Schottky-barrier diodes. First, the absence of even harmonics greatly simplifies the circuit design, particularly in the millimeter-wave region. Also, with the proper pump amplitude the desired harmonic (fifth in this case) has greater available power than other odd harmonics, easing the usual constraint of reactively terminating the lower harmonics to add power to the desired one. Finally, since negative differential resistance is available, the maximum theoretical generation efficiency of a double-barrier diode could possibly be higher than the n^{-2} (n is the harmonic number) value that applies to ideal diodes.[2]

Preliminary quintupling experiments have also been performed in the millimeter-wave region. For example, a conversion efficiency of 0.1 percent was obtained with a pump frequency at 40 GHz and fifth harmonic at 200 GHz. This lower value of conversion efficiency compared with the microwave result reflects the fact that 200 GHz is close to the frequency f_{max} above which the negative resistance of this particular diode vanishes.[3] We believe that f_{max} can be raised to 1 THz with proper material optimization.[4]

<div align="right">

T.C.L.G. Sollner   W.D. Goodhue
E.R. Brown   C.A. Correa

</div>

4.3. EXCIMER-LASER PROJECTION LITHOGRAPHY

Photolithographic techniques, based on image projection with visible/near-UV radiation, play a dominant role in integrated-circuit manufacturing because they provide a unique combination of high precision and low cost. Their extension to shorter wavelengths and higher resolution will be the key to an improving manufacturing technology for smaller devices and greater VLSI complexity. Excimer lasers, operating at 308, 248, and 193 nm, are attractive for use in advanced projection systems.

In the spectral range of greatest interest ($\lambda < 300$ nm), very few properly designed and traditional photoresists have been tested and reported. Extensive testing has been performed elsewhere on Novolak-resin-based, visible/near-UV lamp resists at short wavelengths. Most of these were found to be much too strongly absorbing for good profile control. Furthermore, the absorption does not exhibit photobleaching, often leading to a more sloped profile. We have investigated projection patterning of wet-developed polymethyl methacrylate (PMMA) with ArF-excimer lasers at 193-nm wavelength. We obtained excellent results, as shown in Figure 4-8. Lines and spaces, nominally 130-nm wide, were etched in 150-nm-thick PMMA on silicon. Exposure was with a single, 15-ns-long pulse at $\sim$1-J/cm^2 fluence, followed by 5-min development in a methyl-isobutylketone/isopropanol solution.
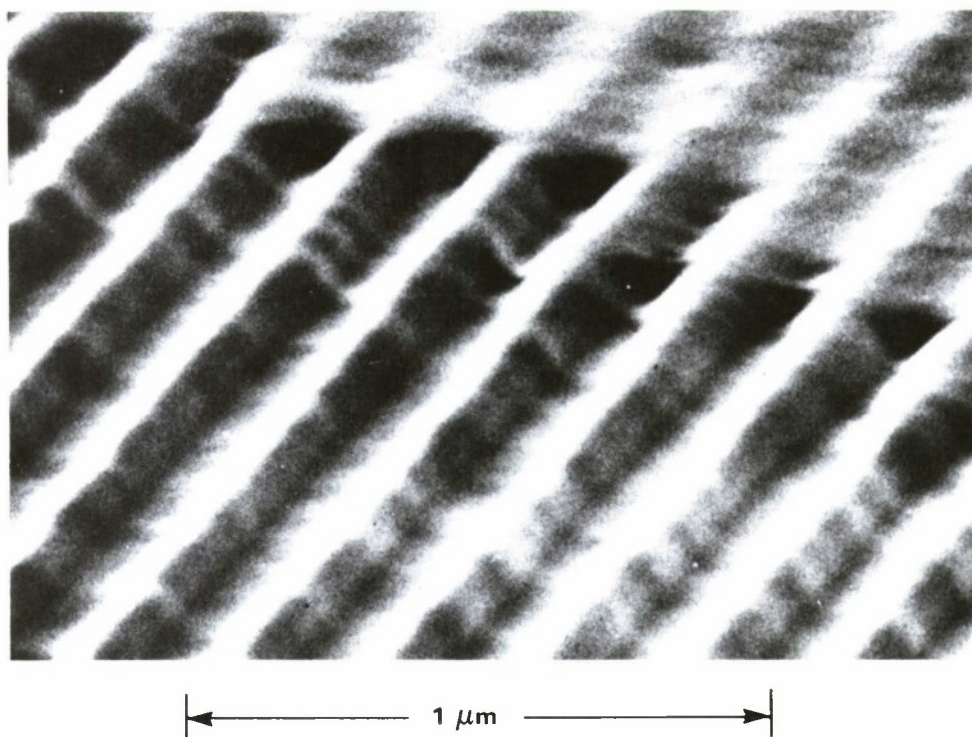
Figure 4-8. SEM of 130-nm lines and spaces patterned in 150-nm-thick PMMA on silicon.

We note the high optimization of this system. The 130-nm-wide lines are significantly smaller than the wavelength of the laser and, in fact, approach the absolute diffraction-limited cutoff width, $\lambda/4NA = 97$ nm, for the 0.5-NA optics. This result demonstrates the great potential in resolution and throughput of properly configured excimer-laser-based photolithographic projection systems.

M. Rothschild

4.4. OBSERVATION OF INTERSUBBAND TRANSITIONS IN COUPLED QUANTUM WELLS

There is growing interest in new devices based on confined states in quantum wells. Absorption between subbands in isolated quantum wells was first observed by West and Eglash.[5] Compared with single quantum wells, coupled quantum wells offer a much richer spectrum of energy levels. In a symmetric coupled-well system, each state of the uncoupled well is split into a lower-energy state with a symmetric wavefunction and a higher-energy state with an antisymmetric wavefunction. We report here the first observation of intersubband transitions between such states in coupled quantum wells.

A diagram of our GaAs/AlGaAs coupled-well structure is shown in Figure 4-9. The intersubband transitions in the conduction band of this coupled-well sample have been studied by

30 PERIODS
~1.6 μm

$Al_{0.3}Ga_{0.7}As$
0.1 μm

$Al_{0.3}Ga_{0.7}As$
0.1 μm

(a)

n^+GaAs
0.5 μm

SI GaAs
SUBSTRATE

• • •

8 nm ⌐ 8 nm

(b)

E_4
E_3
E_2
E_1

12 nm UNDOPED

++++

11 nm
2×10^{18}
cm^{-3}

12 nm UNDOPED

1.5 nm

◄——— ONE PERIOD ———►
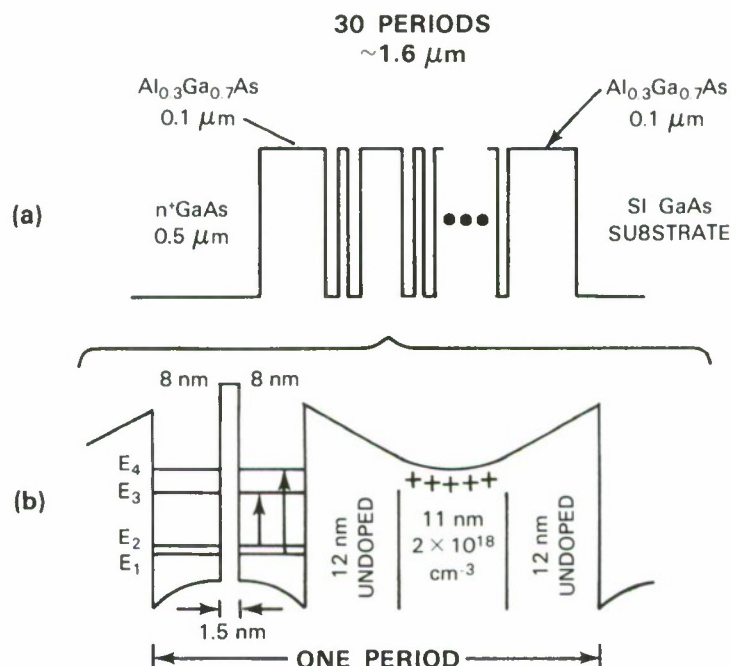
*Figure 4-9. (a) Coupled-well structure estimated from growth conditions.
(b) Expanded view showing allowed transitions and band-bending.*

transmission spectroscopy in the wavelength region of 2 to 25 μm using a Fourier-transform spectrometer. Transmission spectra were taken as the sample was cooled to about 20 K in the dark. When cold, the sample was illuminated with white light for a few seconds and then further spectra were taken. Illumination ionizes DX centers (electron traps) present in the AlGaAs barriers. These electrons are captured in the well, and the additional population in the lower-energy states results in an increase in absorption at the intersubband transition energies. This effect persists after the illumination is turned off.

Transmission spectra from a typical run are shown in Figure 4-10. The top three curves trace variations in absorption as the sample was cooled to 20 K, and the lowest curve shows the increase in absorption after the sample had been illuminated.

We have previously found in single-quantum-well samples that intersubband transition energies increase as the sample is cooled; this results primarily from the slight difference between the temperature coefficients of the bandgaps in the well and barrier layers. In the transmission curves for the coupled wells, three absorption features (labeled A, B, and C) are seen to shift to higher energies as the sample is cooled. These three features also show increased absorption after the sample is illuminated, as seen in the bottom curve in Figure 4-10. This is seen more clearly in Figure 4-11, in which the ratio of the 20-K spectrum after illumination to the 20-K spectrum before illumination has been plotted in order to yield the absorption due to the additional electrons captured from the ionized DX centers. An increase in absorption is also apparent at the

57

Figure 4-10. Transmission spectra from coupled wells. Calculated transition energies are marked with arrows at the bottom of the figure as explained in the text.
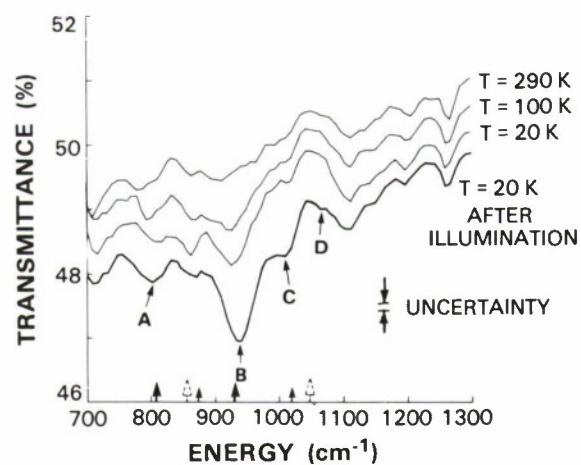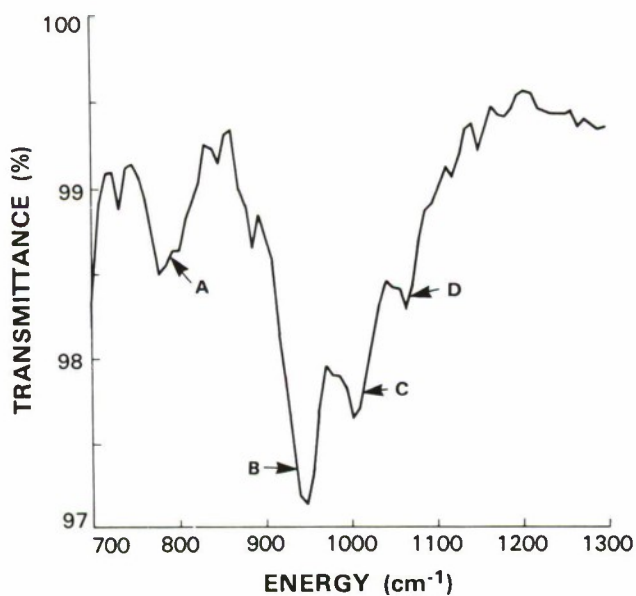

Figure 4-11. Ratio of the 20-K curve of Figure 4-10 after illumination to that before illumination.

58

energy labeled D, although this feature is not obvious before illumination. The shifts with temperature and increased absorption after illumination that are seen at A, B, and C identify these features as resulting from direct intersubband transitions in the coupled quantum wells.

We have calculated energy levels, wavefunctions, and transition probabilities for quantum wells coupled through a barrier. The largest pair of observed absorptions, A and B, are identified with the allowed transitions, E_2 to E_3 and E_1 to E_4, respectively, as defined in Figure 4-9. A structure with the center barrier seven lattice constants thick and the wells fifteen lattice constants thick predicts the observed absorption positions as shown by the large solid arrows in Figure 4-10. (One lattice constant equals 0.56 nm.) The best fit is obtained with a mole-fraction of 29% Al in the barriers. Transition B is expected to be stronger than A since it involves the ground state.

In some spectra taken at other positions on the wafer, transitions A and B were observed at lower energies. These observed energies are consistent with well widths larger by one lattice constant in these regions of the wafer. Transition C corresponds to the higher-energy transition that would be found in a structure with well widths smaller by one lattice constant. The other allowed transition in such a structure would be found at approximately 875 cm^{-1}, perhaps contributing to the small absorption feature there. These calculated positions are marked with small solid arrows on Figure 4-10. The weak absorption labeled D may correspond to the higher-energy transition in a system with both wells and center barrier smaller by one lattice constant. The positions of the two calculated absorptions for this last case are marked with dashed arrows on Figure 4-10.

The structure parameters that best fit the observed absorptions are, in most cases, in agreement with those expected from the growth conditions and those shown in Figure 4-9. The one large discrepancy is the coupling-barrier thickness. It was expected to be three lattice constants thick rather than the fitted value of seven lattice constants. One other feature that needs more analysis is the shift in absorption after illumination. All absorptions move to lower energy except B, which moves to slightly higher energy. We will investigate these issues in the near future.

K.A. McIntosh   W.D. Goodhue
J.W. Bales   T.C.L.G. Sollner

REFERENCES

1. Solid State Research Report, Lincoln Laboratory, MIT (1986:1), p. 27, DTIC AD-A176097.

2. C.H. Page, Proc. IRE **46**, 1738 (1958).

3. E.R. Brown, T.C.L.G. Sollner, W.D. Goodhue, and C.D. Parker, Appl. Phys. Lett. **50**, 83 (1987).

4. T.C.L.G. Sollner, E.R. Brown, W.D. Goodhue, and H.Q. Le, Appl. Phys. Lett. **50**, 332 (1987), DTIC AD-A178910.

5. L.C. West and S.J. Eglash, Appl. Phys. Lett. **46**, 1156 (1985).

5. ANALOG DEVICE TECHNOLOGY

5.1. HIGH-SPEED JOSEPHSON BINARY ADDRESS ENCODER FOR A SUPERCONDUCTIVE CORRELATOR

We recently completed the design, fabrication, and testing of a high-speed Josephson-junction-based digital circuit designed for use in a multichannel, multigigahertz-bandwidth time-integrating correlator.[1] The circuit functions as an address encoder: when the nth input of the N data inputs goes high, the encoder reports the binary representation of n. Thus, the output of the proposed multichannel correlator is reduced from N output lines to $\log_2 (N + 1)$ lines.

The address encoder was designed using 4JL circuitry,[2] configured as an interconnected set of OR gates. The current design, shown in Figure 5-1, provides a binary encoding of up to seven inputs. Using two such encoders, we anticipate constructing a 14-channel time-integrating-correlator device.

The test results from the address encoder are shown in Figure 5-2. It is observed that after the input D5 goes high, the appropriate address outputs A0 and A2 also go high. Note that the power supply is clocked in order to reset the latching OR gates.
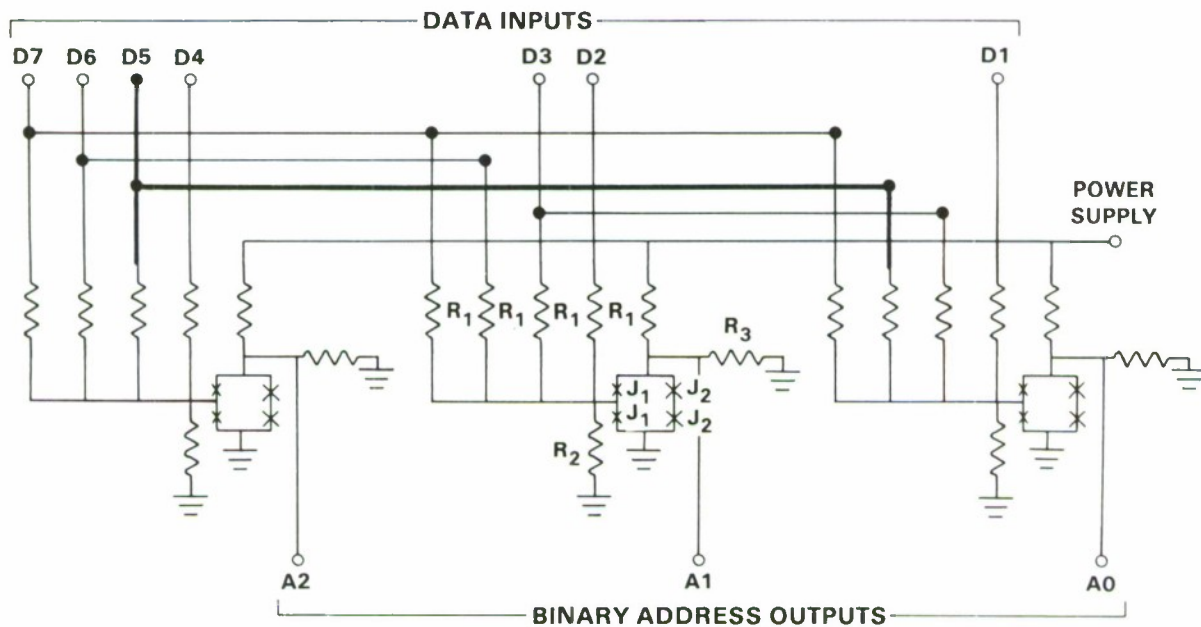
Figure 5-1. Schematic of 7-input address encoder using cross-coupled OR gates constructed with Josephson-junction logic elements.

POWER SUPPLY →

20 mV

DATA INPUT (D5)

10 mV

BINARY ADDRESS OUTPUTS

A2

A1

5 mV

A0

2 μs
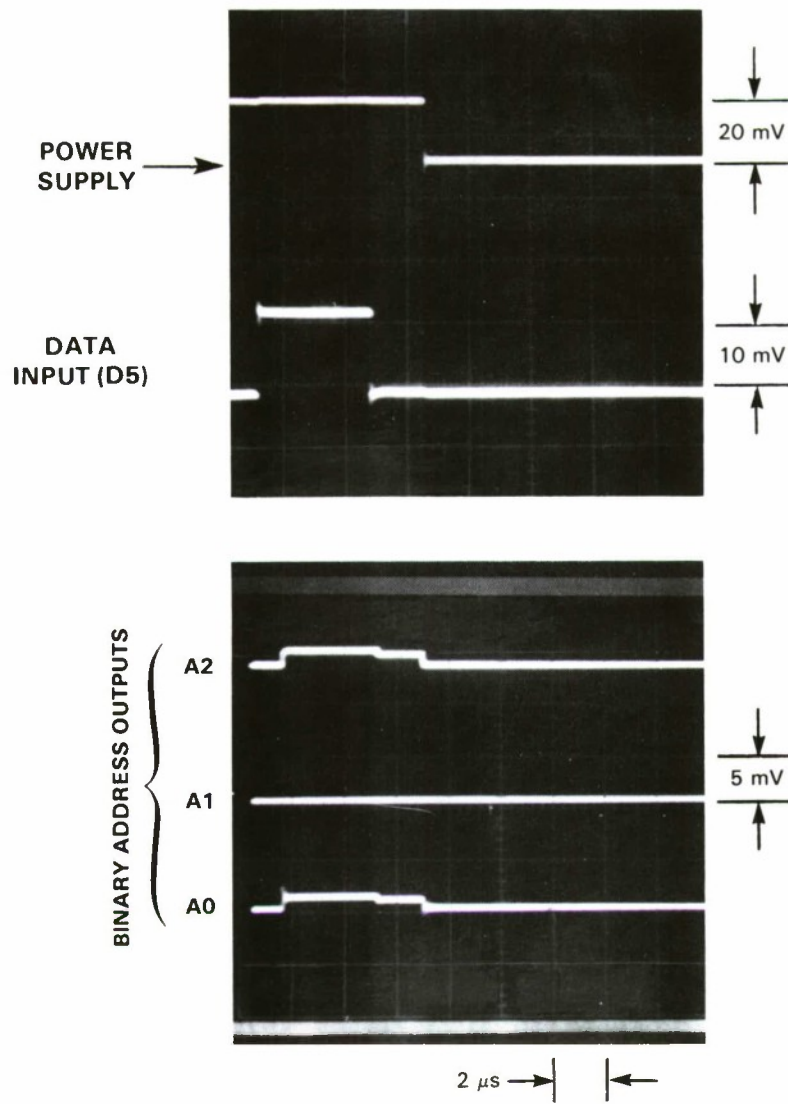
OUTPUT (Binary): 101 → DATA INPUT #5

Figure 5-2.   Operation of superconductive digital address encoder. When input line D5 goes high, its address is properly encoded in binary as 101.

87265-43

62

Simulations were done which showed that the intrinsic switching time of the address encoder is about 150 ps. This switching time was limited by the 5-μm design rules and the high specific capacitance of the $Nb/Nb_2O_5/Pb$ tunnel junctions used for circuit fabrication. If needed, faster circuit operation could be obtained by decreasing the size of the Josephson tunnel junctions. The switching time, measured at the top of the dewar (at the end of a 3-ft probe), was 1.4 ns. This address encoder operation does not push the state of the art of Josephson technology but is adequate for the correlator application.

<div align="right">J.B. Green
A.C. Anderson</div>

5.2. HIGH-PERFORMANCE MOSFET-WEIGHTED SAW/FET PROGRAMMABLE TRANSVERSAL FILTER

The SAW/FET is a wideband programmable transversal filter that uses a surface-acoustic-wave (SAW) delay line for the wideband delay element and a silicon metal-oxide-semiconductor (MOS) integrated circuit for the programmable tap weighting. Substantial design improvements have simplified the processing and have yielded better uniformity, lower insertion loss, and a higher programmable on/off ratio.

The SAW/FET was described in detail previously.[3,4] Briefly, Figure 5-3 shows a $LiNbO_3$ SAW delay line coupled to a Si integrated circuit which contains the programmable analog taps that sample the signal propagating along the SAW delay line. The taps are metal fingers on the silicon substrate capacitively coupled to the piezoelectric field of the SAW across a narrow air gap maintained by SiO_2 rails deposited on the silicon chip. Previous SAW/FETs used MOS varactors (voltage-controlled capacitors) associated with each finger as tap-weighting elements. In the present design, the taps are coupled to a summing bus by a programmable resistive summing network consisting of MOSFETs used as varistors (electrically variable resistors). The varistor weights are programmed by bias voltages introduced through a programming network that is controlled by an on-chip digital shift register. The tap-programming circuit shown in Figure 5-3 uses one less transistor per tap-pair per track than the previous circuit, yet allows a true sequential loading of the analog tap weights. The dual-track structure increases the programmable on/off ratio and provides bipolar programming weights.

The use of varistors rather than varactors to program the tap weights has other advantages as well. The varistors do not require the p-well required by the varactors, yielding a simpler process; also, the varistors have much smaller active area than the varactors and are therefore less sensitive to random defects. Furthermore, the electrical characteristics of the varistors are less affected by traps and surface states. Finally, the varistor conductance varies linearly over a wide range of programming voltage, while the varactor capacitance varies nonlinearly over a narrower voltage range. This simplification and reduction in sensitivity have also increased the fabrication yield of good SAW/FET chips.
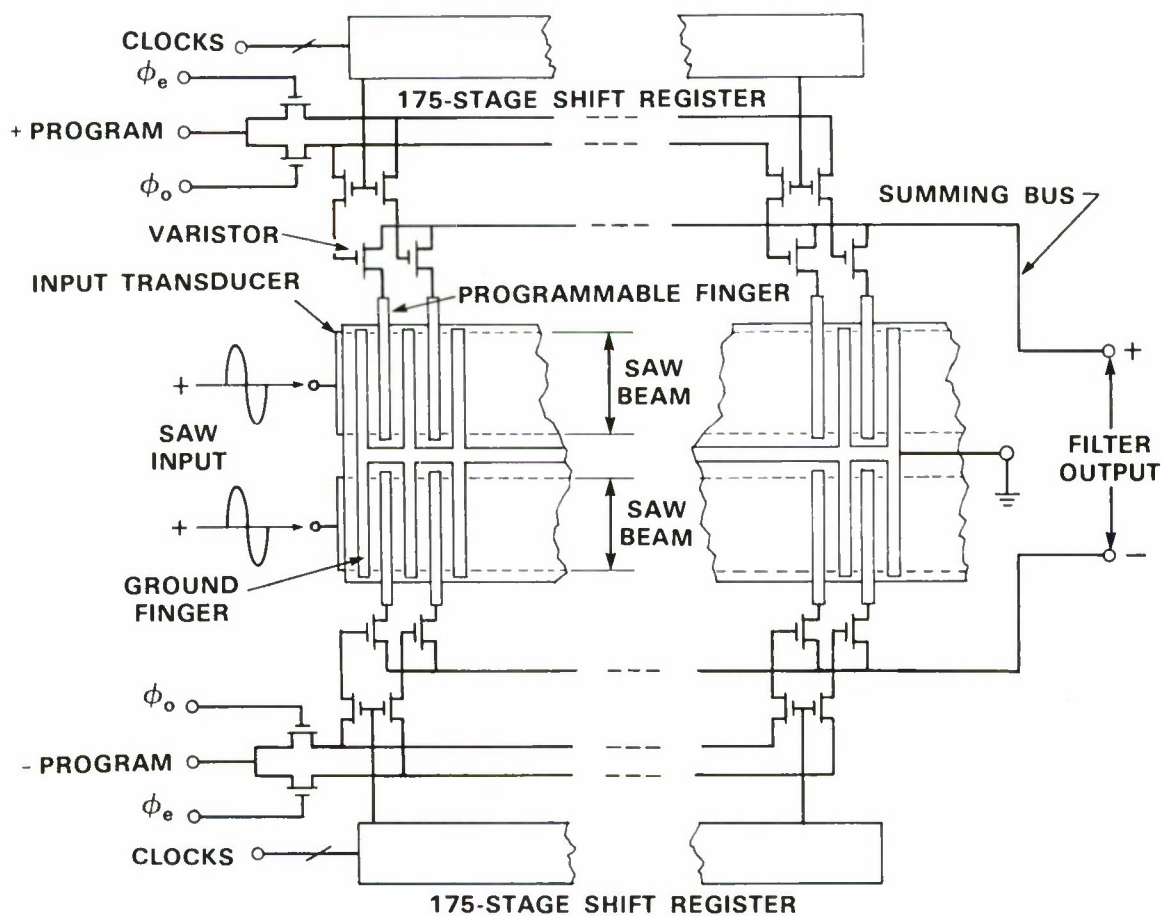
Figure 5-3. Schematic of 350-tap, 100-MHz-bandwidth SAW/FET, including the varistors and improved programming circuitry.

64

Figure 5-4 shows the SAW/FET impulse response when programmed with a square wave such that groups of ten adjacent taps are turned fully on and the next ten adjacent taps are turned off. The top trace shows the programming waveform, the middle trace shows the input RF impulse, and the bottom trace shows the RF output. The on/off ratio is greater than 30 dB, and the tap-to-tap uniformity of ± 1 dB is excellent.

Figure 5-5 shows the frequency response of the SAW/FET when programmed as a narrow-band filter. The sequence of four pictures shows the four different output passbands between 130 and 212 MHz produced by four different programming inputs. The device clearly shows the 100 MHz of programmable bandwidth. The out-of-band rejection is seen to be about 40 dB except for a few isolated frequencies, at which higher spatial harmonics generated by the slightly nonlinear relationship between programming voltage and tap weight are aliased about the 232-MHz effective sampling frequency and appear in band. The insertion loss is less than 40 dB, and the dynamic range over thermal noise is greater than 75 dB with a 27-dBm input signal.

These results show that the new varistor tap-weighting circuitry provides improved on/off ratio, uniformity, linearity, and insertion loss over the previously reported varactor-weighted device. This improvement in performance is achieved with a fabrication procedure for the silicon FET wafers that is simpler and has a higher yield than the procedure required to fabricate the varactor-weighted SAW/FET.

D.L. Smythe   J.B. Green
D.E. Oates   V.S. Dolat

REFERENCES

1. J.B. Green, A.C. Anderson, L.N. Smith, S.A. Reible, and R.S. Withers, IEEE Trans. Magn. **MAG-23**, 895 (1987).

2. H. Nakagawa, E. Sogawa, S. Takada, and H. Hayakawa, "Operating Characteristics of Josephson Direct-Coupled Four Junction Logic (4JL) Gate," Bulletin of the Electrotechnical Laboratory, Sept. 27, 1984.

3. Solid State Research Report, Lincoln Laboratory, MIT (1986:1), p. 47, DTIC AD-A176097.

4. *Ibid.* (1986:4), p. 53, DTIC AD-A182215.

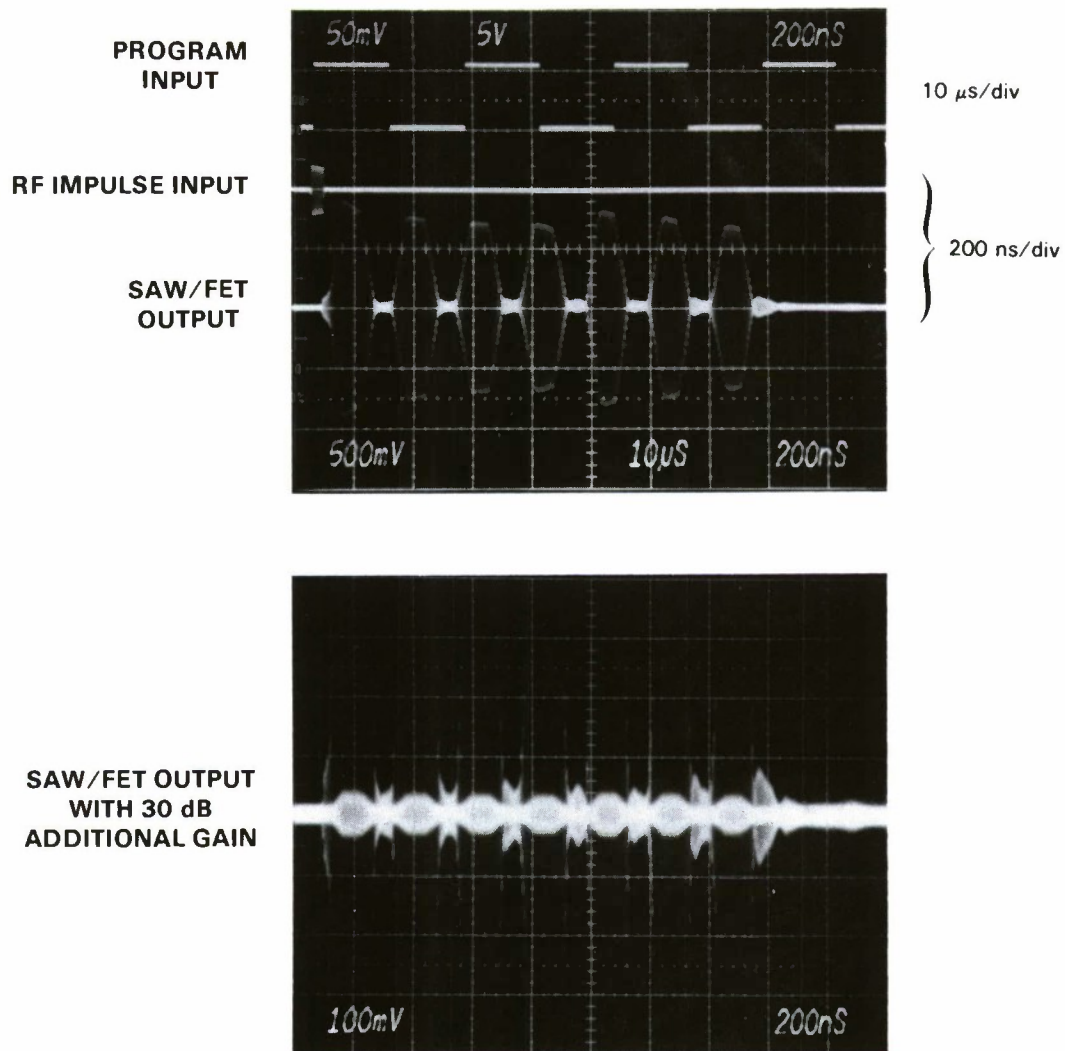Figure 5-4. *Response of the SAW/FET to a short burst of RF. The program input is a square wave that turns on and off alternating groups of adjacent taps. Note the different time scales for the RF input and output and for the programming input.*
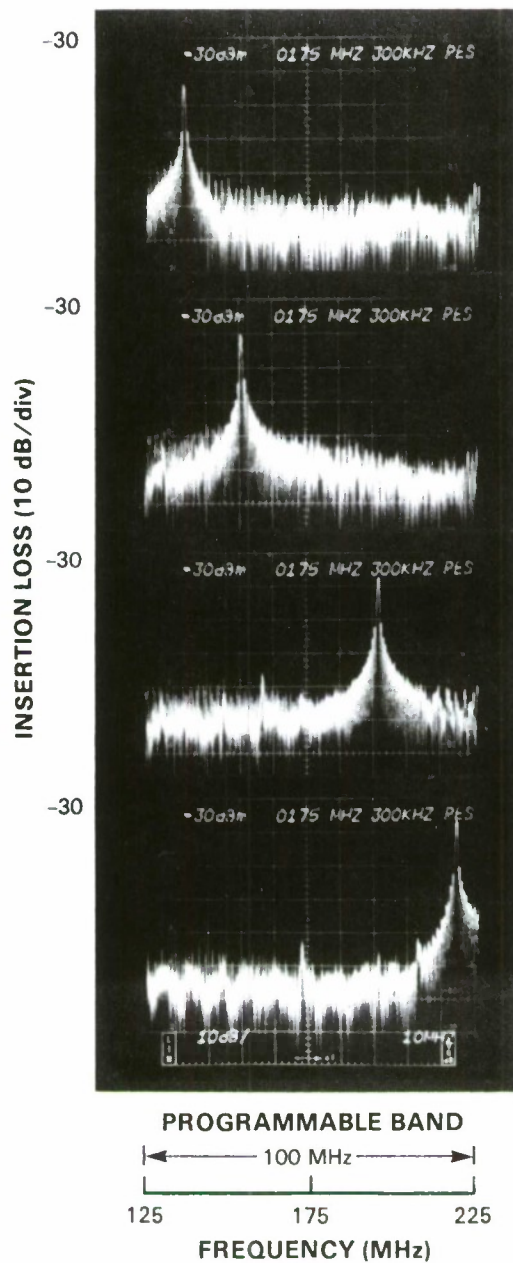
66

Figure 5-5. *Amplitude-vs-frequency response of the SAW/FET programmed as a narrowband filter. Four different program inputs were used to change the center of the passband.*

67

REPORT DOCUMENTATION PAGE

1a. REPORT SECURITY CLASSIFICATION	1b. RESTRICTIVE MARKINGS
Unclassified	

2a. SECURITY CLASSIFICATION AUTHORITY	3. DISTRIBUTION/AVAILABILITY OF REPORT
2b. DECLASSIFICATION/DOWNGRADING SCHEDULE	Approved for public release; distribution unlimited.

4. PERFORMING ORGANIZATION REPORT NUMBER(S)	5. MONITORING ORGANIZATION REPORT NUMBER(S)
1987:3	ESD-TR-87-073

6a. NAME OF PERFORMING ORGANIZATION	6b. OFFICE SYMBOL (If applicable)	7a. NAME OF MONITORING ORGANIZATION
Lincoln Laboratory, MIT		Electronic Systems Division

6c. ADDRESS (City, State, and Zip Code)	7b. ADDRESS (City, State, and Zip Code)
P.O. Box 73 Lexington, MA 02173-0073	Hanscom AFB, MA 01731

8a. NAME OF FUNDING/SPONSORING ORGANIZATION	8b. OFFICE SYMBOL (If applicable)	9. PROCUREMENT INSTRUMENT IDENTIFICATION NUMBER
Air Force Systems Command, USAF		F19628-85-C-0002

8c. ADDRESS (City, State, and Zip Code)	10. SOURCE OF FUNDING NUMBERS			
	PROGRAM ELEMENT NO.	PROJECT NO.	TASK NO.	WORK UNIT ACCESSION NO.
Andrews AFB Washington, DC 20334	63250F	649L		

11. TITLE (Include Security Classification)

Solid State Research

12. PERSONAL AUTHOR(S)
Alan L. McWhorter

13a. TYPE OF REPORT	13b. TIME COVERED	14. DATE OF REPORT (Year, Month, Day)	15. PAGE COUNT
Quarterly Technical Report	FROM 5/1/87 TO 7/31/87	1987, August 15	94

16. SUPPLEMENTARY NOTATION

None

17. COSATI CODES			18. SUBJECT TERMS (Continue on reverse if necessary and identify by block number)
FIELD	GROUP	SUB-GROUP	solid state devices lasers charge-coupled devices
			quantum electronics nonlinear optics microwave semiconductor
			materials research photorefractive effort devices
			microelectronics quantum-well effects silicon-on-insulator devices
			analog device technology superconductors signal processing

19. ABSTRACT (Continue on reverse if necessary and identify by block number)

    This report covers in detail the solid state research work of the Solid State Division at Lincoln Laboratory for the period 1 May through 31 July 1987. The topics covered are Solid State Device Research, Quantum Electronics, Materials Research, Microelectronics, and Analog Device Technology. Funding is provided primarily by the Air Force, with additional support provided by the Army, DARPA, Navy, SDIO, NASA, and DOE.

20. DISTRIBUTION/AVAILABILITY OF ABSTRACT	21. ABSTRACT SECURITY CLASSIFICATION
☐ UNCLASSIFIED/UNLIMITED ☒ SAME AS RPT. ☐ DTIC USERS	Unclassified

22a. NAME OF RESPONSIBLE INDIVIDUAL	22b. TELEPHONE (Include Area Code)	22c. OFFICE SYMBOL
Lt. Col. Hugh L. Southall, USAF	(617) 981-2330	ESD/TML